

Early Planet Formation in Embedded Disks (eDisk) XIV: Flared Dust Distribution and Viscous Accretion Heating of the Disk around R CrA IRS 7B-a

SHIGEHISA TAKAKUWA,^{1,2} KAZUYA SAIGO,¹ MIYU KIDO,¹ NAGAYOSHI OHASHI,² JOHN J. TOBIN,³ JES K. JØRGENSEN,⁴
YURI AIKAWA,⁵ YUSUKE ASO,⁶ SACHA GAVINO,⁴ ILSEUNG HAN,^{7,6} PATRICK M. KOCH,² WOJIN KWON,^{8,9}
CHANG WON LEE,^{7,6} JEONG-EUN LEE,¹⁰ ZHI-YUN LI,¹¹ ZHE-YU DANIEL LIN,¹¹ LESLIE W. LOONEY,¹² SHOJI MORI,¹³
JINSHI SAI (INSA CHOI),² RAJEEB SHARMA,⁴ PATRICK SHEEHAN,³ KENGO TOMIDA,¹³ JONATHAN P. WILLIAMS,¹⁴
YOSHIHIDE YAMATO,⁵ AND HSI-WEI YEN²

¹Department of Physics and Astronomy, Graduate School of Science and Engineering, Kagoshima University, 1-21-35 Korimoto, Kagoshima, Kagoshima 890-0065, Japan

²Academia Sinica Institute of Astronomy & Astrophysics, 11F of Astronomy-Mathematics Building, AS/NTU, No.1, Sec. 4, Roosevelt Rd, Taipei 10617, Taiwan, R.O.C.

³National Radio Astronomy Observatory, 520 Edgemont Rd., Charlottesville, VA 22903 USA

⁴Niels Bohr Institute, University of Copenhagen, Øster Voldgade 5–7, DK 1350 Copenhagen K., Denmark

⁵Department of Astronomy, Graduate School of Science, The University of Tokyo, 7-3-1 Hongo, Bunkyo-ku, Tokyo 113-0033, Japan

⁶Korea Astronomy and Space Science Institute, 776 Daedeok-daero, Yuseong-gu, Daejeon 34055, Republic of Korea

⁷Division of Astronomy and Space Science, University of Science and Technology, 217 Gajeong-ro, Yuseong-gu, Daejeon 34113, Republic of Korea

⁸Department of Earth Science Education, Seoul National University, 1 Gwanak-ro, Gwanak-gu, Seoul 08826, Republic of Korea

⁹SNU Astronomy Research Center, Seoul National University, 1 Gwanak-ro, Gwanak-gu, Seoul 08826, Republic of Korea

¹⁰Department of Physics and Astronomy, Seoul National University, 1 Gwanak-ro, Gwanak-gu, Seoul 08826, Korea

¹¹University of Virginia, 530 McCormick Rd., Charlottesville, Virginia 22904, USA

¹²Department of Astronomy, University of Illinois, 1002 West Green St, Urbana, IL 61801, USA

¹³Astronomical Institute, Graduate School of Science, Tohoku University, Sendai 980-8578, Japan

¹⁴Institute for Astronomy, University of Hawai'i at Mānoa, 2680 Woodlawn Dr., Honolulu, HI 96822, USA

ABSTRACT

We performed radiative transfer calculations and observing simulations to reproduce the 1.3-mm dust-continuum and C¹⁸O (2–1) images in the Class I protostar R CrA IRS7B-a, observed with the ALMA Large Program “Early Planet Formation in Embedded Disks (eDisk)”. We found that the dust disk model passively heated by the central protostar cannot reproduce the observed peak brightness temperature of the 1.3-mm continuum emission (~ 195 K), regardless of the assumptions about the dust opacity. Our calculation suggests that viscous accretion heating in the disk is required to reproduce the observed high brightness temperature. The observed intensity profile of the 1.3-mm dust-continuum emission along the disk minor axis is skewed toward the disk far side. Our modeling reveals that such an asymmetric intensity distribution requires flaring of the dust along the disk’s vertical direction with the scale-height following $h/r \sim r^{0.3}$ as function of radius. These results are in sharp contrast to those of Class II disks, which show geometrically flat dust distributions and lower dust temperatures. From our modeling of the C¹⁸O (2–1) emission, the outermost radius of the gas disk is estimated to be ~ 80 au, larger than that of the dust disk (~ 62 au), to reproduce the observed distribution of the C¹⁸O (2–1) emission in IRS 7B-a. Our modeling unveils a hot and thick dust disk plus a larger gas disk around one of the eDisk targets, which could be applicable to other protostellar sources in contrast to more evolved sources.

Keywords: Interstellar medium (847); Planet formation (1241); Radiative transfer (1335); Star formation (1569)

1. INTRODUCTION

The ALMA Large Program “Early Planet Formation in Embedded Disk (eDisk)” has newly observed eleven Class 0 and six Class I protostars in 1.3-mm dust continuum and selected molecular lines, including $C^{18}O$ (2–1), around 230 GHz at a spatial resolution of ~ 7 au (plus one Class 0 and I sources from archival data). The datasets enable us to investigate the ongoing disk and planet formation occurring during the protostellar stages systematically (Ohashi et al. 2023). As reported in the present series of the eDisk first-look papers, the initial results have demonstrated intriguing features of the protostellar disks, envelopes, and outflows. For example, eDisk has unveiled that Keplerian rotating disks are often found even in the Class 0 stage (van’t Hoff et al. 2023; Kido et al. 2023; Sharma et al. 2023; Aso et al. 2023; Sai et al. 2023; Thieme et al. 2023). While concentric ring and gap features, often seen in Class II disks (e.g., Andrews et al. 2018), are only seen toward the most evolved eDisk sources of Oph IRS 63 (Flores et al. 2023) and L1489 IRS (Yamato et al. 2023), “bump” or “shoulder” features are seen in Class 0 sources of Ced 110 IRS 4 (Sai et al. 2023) and CB 68 (Kido et al. 2023). In the envelopes, flow-like molecular gas accreting toward the central protostellar disks, accretion streamers, have been identified (Kido et al. 2023; Aso et al. 2023; Flores et al. 2023; Han et al. 2023b). An extended circumbinary envelope around the compact binary disks is also identified (Narayanan et al. 2023).

To put these observational results into a quantitative astrophysical context, we need to compare the observations to detailed synthetic observations based on radiative transfer modeling of protostellar disks and envelopes (see Baek et al. 2020) properly processed with simulations of the ALMA imaging process. In this paper, we report our first attempt to reproduce the observed 1.3-mm continuum and $C^{18}O$ (2–1) emission in one of the eDisk targets; R CrA IRS 7B (Groppi et al. 2007; Peterson et al. 2011; Lindberg & Jørgensen 2012; Lindberg et al. 2014a,b). R CrA IRS 7B is a Class I protostar located in Corona Australis, with a bolometric luminosity of $L_{\text{bol}} = 5.1 L_{\odot}$ and a bolometric temperature of $T_{\text{bol}} = 88$ K, which are reestimated using the archival photometric data by the eDisk team (see Ohashi et al. 2023, for details). Note that both in terms of its bolometric luminosity and temperature R CrA IRS 7B is typical among the eDisk targets. The distance to the source is estimated to be 152 pc based on the GAIA data (Galli

et al. 2020). Previous SMA and ALMA observations of R CrA IRS 7B demonstrated the presence of compact 1.3-mm and 0.8-mm continuum emission (Lindberg & Jørgensen 2012; Lindberg et al. 2014b). Through ALMA observations of the $C^{17}O$ (3–2) line, a velocity gradient along the major axis of the dust emission was identified, which is interpreted as the signature of Keplerian rotation (Lindberg et al. 2014b). The angular resolutions of these previous observations are, however, not sufficient to investigate the detailed internal structure of the protostellar disk. The eDisk observations for the first time revealed that R CrA IRS 7B consists of two sources; one to the southeast (R CrA IRS 7B-a) and the other to the northwest (R CrA IRS 7B-b), each surrounded by a separate dust disk (Ohashi et al. 2023). In the present paper, we focus on the southeastern source, R CrA IRS 7B-a, which is referred to as IRS 7B-a hereafter.

Figure 1 shows the entire and zoom-in views of the observed 1.3-mm dust-continuum emission in IRS 7B-a (Ohashi et al. 2023). The peak brightness temperature of the 1.3-mm dust-continuum emission is as high as ~ 195 K. It is clear that along the minor axis, the emission gradient toward the northeast is steeper than toward the southwest, suggesting the presence of asymmetry (Figure 1 right). Ohashi et al. (2023) also found that the $C^{18}O$ (2–1) emission shows a signature of the Keplerian rotation in the disk with an inferred central protostellar mass of $2.1\text{--}3.2 M_{\odot}$, while the emission becomes weaker at the disk center against the bright dust continuum emission.

Similar characteristics are also seen in several other eDisk sources, and thus it is important to reproduce these features with radiative transfer modeling and to study the physical causes of such characteristics. Our approach is, however, not to construct elaborated theoretical models of the protostellar system or perform quantitative fitting of the model to the observed images. Instead, we aim to construct a simple, but sufficient, physical model that can reproduce these observed characteristic features as quantitatively as possible. Such an approach enables us to discuss the primary causes of the observed features and the important insights behind them.

The structure of the present paper is as follows. In Section 2 physical models of the disk and envelope are described, followed by a detailed explanation of the radiative transfer calculations and the model parameter

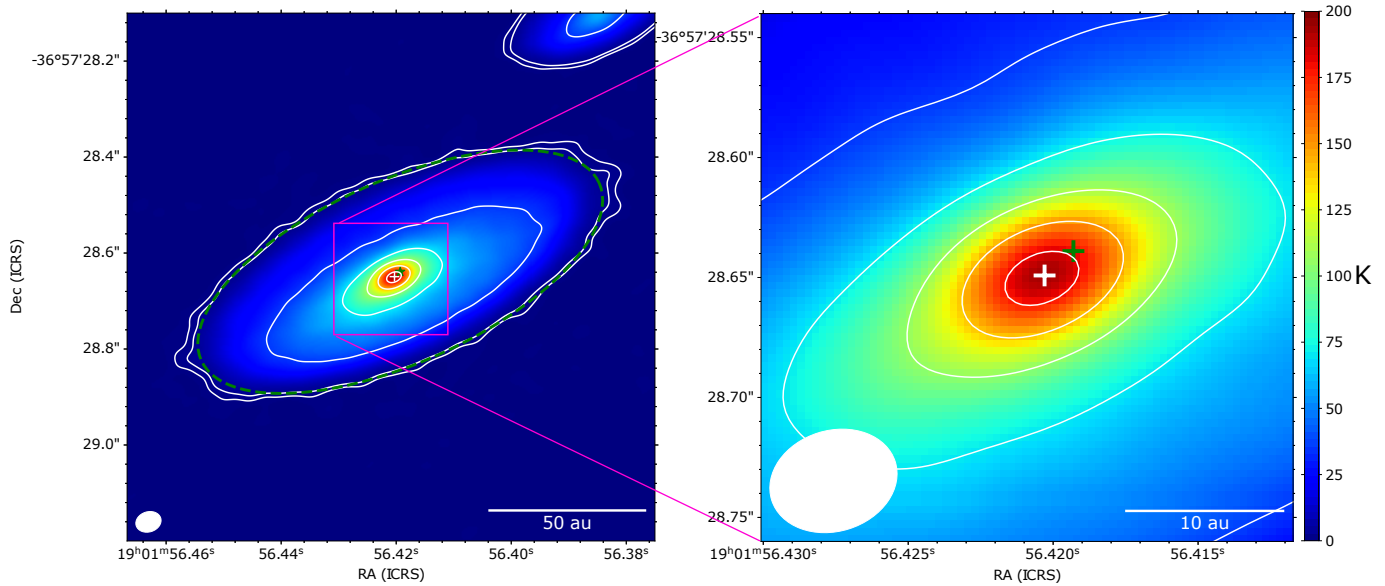


Figure 1. Overall (*left*) and zoom-in images (*right*) of the observed 1.3-mm dust continuum emission in IRS 7B-a. Solid contours show 5σ , 9σ , 100σ , 200σ , 300σ , 400σ , and 500σ ($\sigma = 0.033 \text{ mJy beam}^{-1} = 0.36 \text{ K}$). The beam size is $0''.054 \times 0''.042$ (P.A. = -72.6°). A white cross denotes the peak position of the 1.3-mm dust continuum emission, whose coordinates are $(19^{\text{h}}01^{\text{m}}56^{\text{s}}.420, -36^\circ57'28''.65)$. This position is adopted as the origin of the intensity profile and the position-velocity diagrams. For reference, a green cross is an approximate geometrical center of the ellipse (dashed green line), which delineates the contour with the intensity of $0.3 \text{ mJy beam}^{-1}$.

search. In Section 3 the model images of the 1.3-mm dust continuum emission with a range of model parameters are compared to the real observed 1.3-mm image. Physical causes of the high observed brightness temperature of the 1.3-mm dust continuum emission and the asymmetric intensity profile along the disk minor axis are discussed separately. In Section 4 the model C^{18}O velocity channel maps and P-V diagrams are compared to those of the real data. In Section 5 we discuss implications of our modeling results in the context of the evolution of disks into planet formation. Section 6 gives a concise summary of the present work.

2. MODEL

We introduce protostellar disk + envelope models which should be able to capture the main observed features with the minimum model complexity. The gas and dust distributions are assumed to be azimuthally symmetric as well as mirror-symmetric with respect to the midplane. The spatial grids in a spherical polar coordinate system are $(r, \theta, \phi) = (512, 512, 1)$. In the radial direction, an equally spaced grid on a logarithmic scale is adopted. In the polar direction a linearly equally-spaced grid is adopted. In our preliminary parameter search, a coarser grid of $(256, 256, 1)$ is also adopted for efficient calculations. The radius r and elevation angle θ range $r = 1.0 - 20000 \text{ au}$ and $\theta = 0^\circ - 90^\circ$, respec-

tively. The innermost radius of 1 au is fine enough for the spatial resolution of the observed images ($\sim 7 \text{ au}$). An even smaller inner radius makes the gas temperature too high, and the collisional coefficients of C^{18}O unavailable. Within this defined space our model includes three distinct components; a Keplerian disk, a rotating and infalling protostellar envelope surrounding the disk, and a static “cocoon” of molecular gas surrounding the envelope. The cocoon is a spherical shell with a constant gas density of 10^4 cm^{-3} between $r=10000 \text{ au}$ and 20000 au that mimics the ambient molecular cloud component. No gas motion except for an isotropic turbulence of 0.2 km s^{-1} is included in the cocoon.

2.1. Keplerian Disk

The implementation of the Keplerian disk is similar to that by Kwon et al. (2015) and Ichikawa et al. (2021). The disk properties are calculated with the cylindrical radius R ,

$$R = r \sin \theta. \quad (1)$$

The vertical scale height h_0 of dust and gas at $R = R_0$ is set to be

$$h_0 = \frac{c_{s0}}{\Omega_{K0}}, \quad (2)$$

where

$$c_{s0} = \sqrt{\frac{k_{\text{B}} T_0}{m_{\text{p}} \mu}}, \quad (3)$$

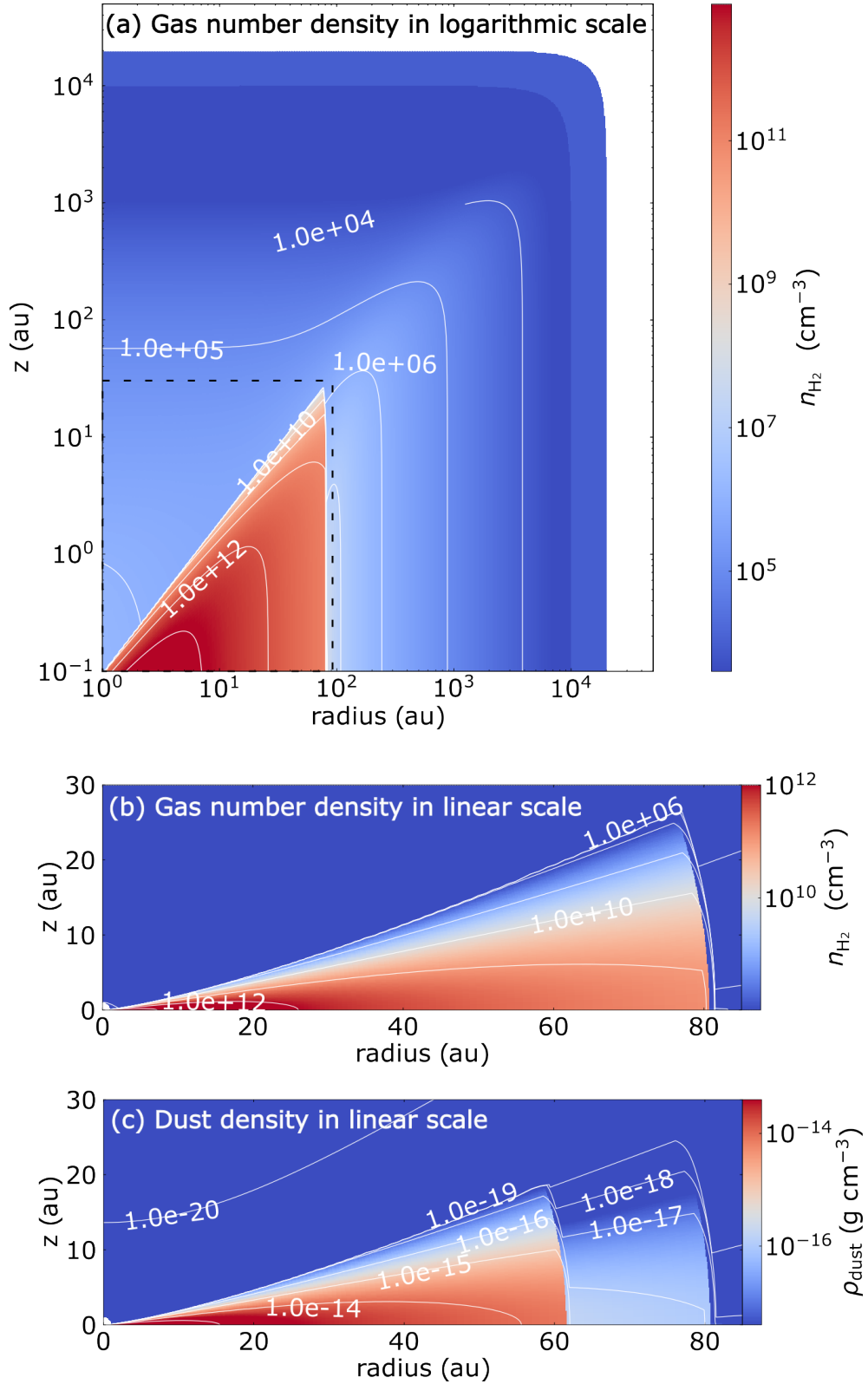


Figure 2. a) Distribution of the gas number density ($\equiv n_{\text{H}_2}$) of the fiducial model in the $\log R - \log z$ plane. The high-density region represents the disk, and the region outside the disk represents the protostellar envelope. In the outermost part of the envelope, a static, uniform cocoon with $n_{\text{H}_2} = 10^4 \text{ cm}^{-3}$ is present. Contour levels start from 10^4 cm^{-3} in steps of a factor of 10. A black dashed rectangle delineates the zoom-in region shown in panels b and c. b) Zoom-in view of the n_{H_2} distribution in the disk region in the $R - z$ plane. Contour levels start from 10^6 cm^{-3} in steps of a factor of 10. c) Same as panel b) but for the distribution of the dust density, ρ_{dust} . Note the shorter outermost radius of the dust disk. Contour levels start from $10^{-20} \text{ g cm}^{-3}$ in steps of a factor of 10.

and

$$\Omega_{K_0} = \sqrt{\frac{GM_\star}{R_0^3}}, \quad (4)$$

are the sound speed and the Keplerian angular velocity in the midplane, respectively, at a reference radius $R_0 = 1$ au, and where k_B denotes the Boltzmann constant, T_0 the midplane dust temperature at R_0 , m_p the proton mass, μ ($=2.33$) the mean molecular weight, G the gravitational constant, and M_\star the stellar mass. M_\star is derived to be in the range of $\sim 2.1 - 3.2 M_\odot$ from the analysis of the observed Position-Velocity diagram in the $C^{18}O$ (2–1) emission (Ohashi et al. 2023), using the SLAM package (Aso & Sai 2023). In our model $M_\star = 2.9 M_\odot$ is adopted, which provides a good match of the model velocity channel maps with the observed velocity channel maps in the $C^{18}O$ emission (see section 4). We set $T_0 = 400$ K, which is simply adopted to calculate the scale height. The true gas and dust temperature will be calculated later with a given density distribution. The radial profile of the scale height ($\equiv h(R)$), or the disk flaring, is expressed as;

$$\frac{h(R)}{R} = \frac{h_0}{R_0} \left(\frac{R}{R_0} \right)^q, \quad (5)$$

where q denotes the disk flaring index.

The gas surface density profile $\Sigma(R)$ is assumed to follow the power-law profile as

$$\Sigma(R) = \Sigma_0 \left(\frac{R}{R_0} \right)^p, \quad (6)$$

where Σ_0 is the surface density at $R = R_0$, and p is the power-law index. p is normally assumed to be in the range between -0.5 and -1 , and here $p = -0.5$ is adopted. The disk is sharply truncated at the inner spherical radius $r < r_{in}$ ($= 1$ au) and the outer radius $r > r_{gas}$. Σ_0 is then derived from the disk mass ($\equiv M_d$) as

$$\Sigma_0 = \frac{(2+p)R_0^p M_d}{2\pi(r_{gas}^{2+p} - r_{in}^{2+p})}. \quad (7)$$

The gas mass density ρ can be described as

$$\rho(R, z) = \frac{\Sigma(R)}{h(R)\sqrt{2\pi}} \exp\left(-\frac{1}{2} \left(\frac{z}{h(R)}\right)^2\right). \quad (8)$$

The velocity field in the disk is a simple Keplerian rotation, expressed as;

$$v_\phi = \sqrt{\frac{GM_\star}{r}}. \quad (9)$$

The gas-to-dust mass ratio is assumed to be 100. During our modeling effort to reproduce both the 1.3-mm

dust-continuum and $C^{18}O$ (2–1) emission, we found, however, that the radius of the dust disk is likely smaller than that of the gas disk (see Section 4). Thus, we introduce an additional parameter, r_{dust} , the radius of the dust disk. Between r_{dust} and r_{gas} , the gas-to-dust mass ratio is arbitrarily enhanced by a factor of 50 to mimic a dust-free region of molecular gas (see section 2.4). The $C^{18}O$ abundance is assumed to be the canonical value of 1.76×10^{-7} (Crapsi et al. 2004) and constant in the disk as well as in the envelope. As shown below, the calculated dust temperature in the disk is above the CO freeze-out temperature of 25 K in most parts of the disk, and thus the constant CO abundance is a reasonable assumption.

2.2. Protostellar Envelope

In the radial range from r_{gas} to $r = 10000$ au, and above $z > 4 \times h$ at $r_{in} \leq r < r_{gas}$, the protostellar envelope of molecular gas and dust is filled. The gas-to-dust mass ratio is assumed to be 100 throughout the envelope as well as the cocoon. The choice of the vertical boundary between the disk and envelope at $4 \times h$ is somewhat arbitrary. If the boundary is set to be $1 \times h$, the model disk is too thin to show the effect of the disk flaring. We also note that the inclusion of the envelope component is important, even if the observed 1.3-mm dust-continuum and the $C^{18}O$ (2–1) emission appear to primarily trace the protostellar disk. As we will show below, inclusion of viscous accretion heating is likely required to reproduce the intense 1.3-mm dust-continuum emission originating from the disk. The protostellar envelope should supply the accreting material to the disk. Furthermore, the presence of the protostellar envelope acts as a ‘‘blanket’’ for the disk by slowing down the escape of photons from the disk.

The model of the rotating and infalling protostellar envelope is taken from Ulrich (1976); Hartmann et al. (1994), and Mendoza et al. (2004). It is a ballistic solution to the two-body problem, with the envelope material following parabolic trajectories around the central protostar. The velocity vector in the 3-dimensional space is expressed as:

$$v_r = - \left(\frac{GM_\star}{r} \right)^{\frac{1}{2}} \left(1 + \frac{\cos \theta}{\cos \theta_0} \right)^{\frac{1}{2}}, \quad (10)$$

$$v_\theta = \left(\frac{GM_\star}{r} \right)^{\frac{1}{2}} \left(\frac{\cos \theta_0 - \cos \theta}{\sin \theta} \right) \left(1 + \frac{\cos \theta}{\cos \theta_0} \right)^{\frac{1}{2}}, \quad (11)$$

$$v_\phi = \left(\frac{GM_\star}{r} \right)^{\frac{1}{2}} \frac{\sin \theta_0}{\sin \theta} \left(1 - \frac{\cos \theta}{\cos \theta_0} \right)^{\frac{1}{2}}, \quad (12)$$

where θ_0 denotes the initial elevation angle of the infalling material. Once the envelope material enters the

disk boundary (see above), the material is assumed to be incorporated into the disk. In the case of the isotropic infall in the envelope, the above infalling velocity yields the expression of the envelope density as;

$$\rho(r, \theta) = \rho_0 \left(\frac{r}{r_{gas}} \right)^{-\frac{3}{2}} \left(1 + \frac{\cos \theta}{\cos \theta_0} \right)^{-\frac{1}{2}} \times \left(3 \frac{r_{gas}}{r} \cos^2 \theta_0 + 1 - \frac{r_{gas}}{r} \right)^{-1}, \quad (13)$$

where

$$\rho_0 = \frac{\dot{M}}{4\pi} \sqrt{\frac{1}{GM_\star r_{gas}^3}}, \quad (14)$$

and \dot{M} indicates the mass infalling rate of the envelope. Note that given M_\star and r_{gas} , the density structure of the envelope is uniquely determined by \dot{M} .

The formulation proposed by [Hartmann et al. \(1994\)](#) is adopted to express the flattening of the envelope as;

$$\rho_{flat}(r, \theta) = \frac{\eta_f}{\cosh^2(\eta_f \cos \theta_0) \tanh \eta_f} \rho(r, \theta), \quad (15)$$

where η_f represents the degree of flattening of the envelope. $\eta_f = 1$ denotes no flattening, *i.e.*, $\rho_{flat}(r, \theta) = \rho(r, \theta)$, while higher values of η_f indicate more flattening. We adopt $\eta_f = 2$, following [Momose et al. \(1998\)](#).

Figure 2a and b show distributions of the volume gas density n_{H_2} (cm^{-3}) in the envelope plus the cocoon and the disk, respectively, of our fiducial model. Figure 2c shows the distribution of the dust density in the disk. The difference of the radii between the molecular and dust disks is presented. The envelope mass of the fiducial model is $0.062 M_\odot$, in contrast with the disk gas mass of $0.41 M_\odot$. The cocoon mass is $1.9 M_\odot$.

2.3. Radiative Transfer Calculations

With these gas and dust density distributions, radiative transfer calculations to produce images of the 1.3-mm dust-continuum and C^{18}O (2–1) emission are conducted using RADMC-3D ([Dullemond 2012](#)). The RADMC-3D calculations involve three separate steps; 1) thermal Monte Carlo simulations to obtain the spatial dust temperature distribution self-consistently, radiative transfer calculations to produce images of 2) the dust-continuum emission and 3) the emission from the C^{18}O (2–1) line. To perform the thermal Monte Carlo simulations, it is required to specify the properties of the central heating source (*i.e.*, protostar), number of photons, wavelength-dependent dust opacity, and if necessary spatial distribution of the internal heating rate. RADMC-3D requires the flux density and radius to specify the central protostar in general. For simplicity, the radiation from the protostar is assumed to be blackbody radiation from

a point source. In such a case, RADMC-3D requires the blackbody temperature only. The relation between the blackbody temperature ($\equiv T_\star$) and the protostellar luminosity ($\equiv L_\star$) is expressed as

$$T_\star = \left(\frac{L_\star}{4\pi R_\star^2 \sigma_{sb}} \right)^{\frac{1}{4}}, \quad (16)$$

where R_\star and σ_{sb} denote the protostellar radius and Stefan–Boltzmann constant, respectively. L_\star is set to be the bolometric luminosity of IRS 7B-a ($= 5.2 L_\odot$)¹ and $R_\star = 1 R_\odot$, which gives $T_\star = 8714$ K. We note that L_{bol} is not strictly the same as L_\star . L_{bol} is derived from the SED fitting over the NIR to millimeter wavelengths ([Ohashi et al. 2023](#)). The NIR emission originated from the protostellar sphere should be attenuated by the surrounding disk, envelope and the ambient gas. On the other hand, the attenuated NIR radiation should be re-emitted at longer wavelengths. As a total radiation energy L_{bol} is still a reasonable proxy of L_\star . To estimate the error of L_{bol} , we tried a new SED fitting using only the data points with the highest value at each wavelength (see Figure 9 in [Ohashi et al. 2023](#)). The derived L_{bol} is $8.3 L_\odot$, $\sim 60\%$ increase from the adopted value of $L_{bol} = 5.2 L_\odot$. As shown below, this highest possible value of L_{bol} is still too low to reproduce the observed high brightness temperature of the 1.3-mm dust continuum emission.

Note that with a given L_\star , R_\star and T_\star are degenerate, and larger R_\star yields lower T_\star . $R_\star = 1 R_\odot$ is likely a lower limit of the protostellar radius, so T_\star is likely an upper limit. The background of this parameter choice is the observed bright 1.3-mm dust-continuum emission. As we will describe below, we have found that the observed bright 1.3-mm dust-continuum emission cannot be reproduced with the heating from the central protostar only, and that internal heating in the disk is likely required. As RADMC-3D only requires the central blackbody temperature to calculate the heating from the central protostar, we set this temperature to a high value. We also attempted even higher luminosities and thus higher blackbody temperatures in our parameter search.

The dust mass opacity is also important but rather uncertain. To convert the observed 1.3-mm flux densities to the dust masses, eDisk papers adopt the Beckwith opacity, which gives $\kappa_{1.3\text{mm}} = 2.3 \text{ cm}^2 \text{ g}^{-1}$ with $\beta =$

¹ During our modeling effort the source bolometric luminosity derived by the eDisk team was $5.2 L_\odot$, which was later updated to $5.1 L_\odot$ ([Ohashi et al. 2023](#)). Since the small difference of the luminosity yields a negligible difference of the stellar radius from $1.0 R_\odot$ to $0.99 R_\odot$ to have the same T_\star , in the present paper, we adopt $5.2 L_\odot$ as the canonical value of the stellar luminosity.

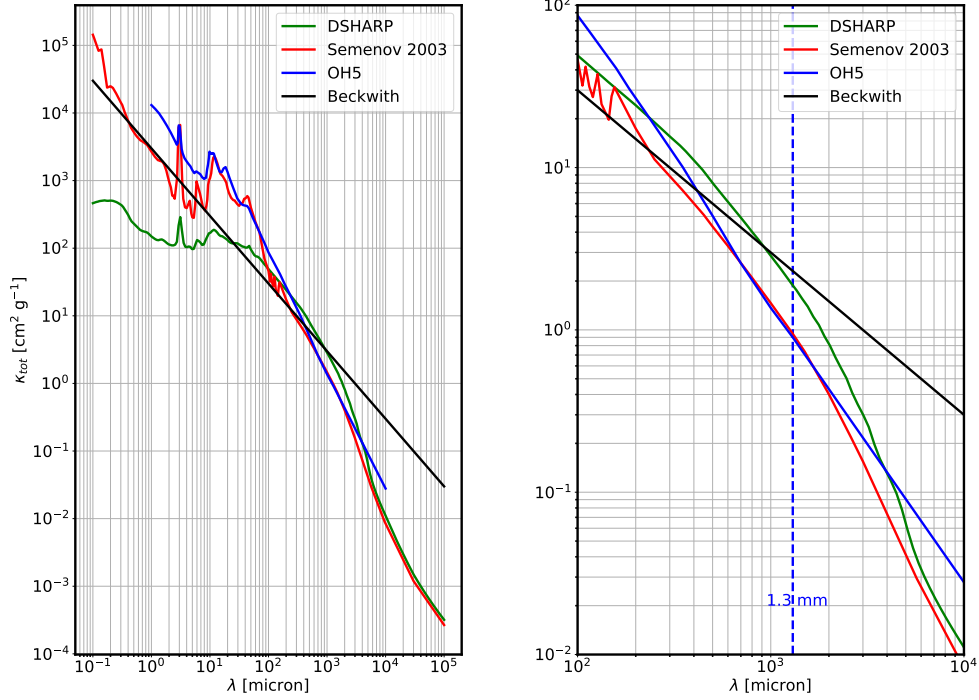


Figure 3. (Left) Dust mass opacity (absorption and scattering) κ_{tot} ($\text{cm}^2 \text{g}^{-1}$) as a function of the wavelength of the four dust models; DSHARP, Semenov, OH5, and Beckwith. (Right) Zoom-in view of the left panel in the submillimeter and millimeter wavelength.

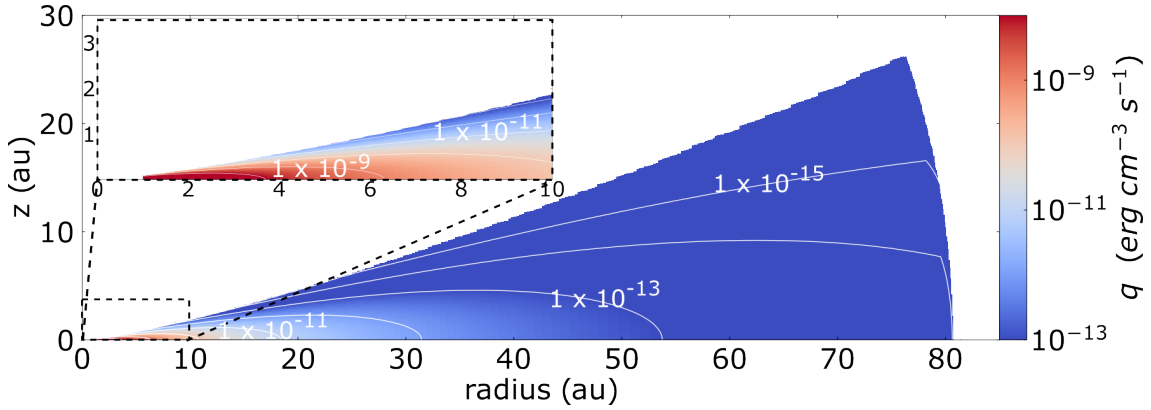


Figure 4. Distribution of the internal heating rate q_{heat} by the viscous accretion heating of the fiducial model, where $\dot{M} = 1.4 \times 10^{-6} (M_{\odot} \text{yr}^{-1})$. Contour levels start from $10^{-15} \text{ erg cm}^{-3} \text{ s}^{-1}$ in steps of a factor of 10.

1 (Beckwith et al. 1990). This $\kappa_{1.3\text{mm}}$ value is similar to the values inferred in the disks around the Class 0 source HH 212 mms (Lin et al. 2021) and the Class I source IRAS 04302+2247 (Lin et al. 2023a). The Beckwith opacity is similar to the opacity with a maximum grain size of 1 mm at millimeter wavelengths (Andrews et al. 2011; Birnstiel et al. 2018; Han et al. 2023a). Another adopted opacity in our modeling is the so-called DSHARP opacity (Birnstiel et al. 2018). While a variety of DSHARP opacity tables can be obtained depending on the assumed dust parameters, the adopted DSHARP

opacity in our models is the same as that shown in the blue curve in Figure 6 by Birnstiel et al. (2018). The adopted opacity is an average over grain sizes from 0.1 μm to 1 mm with a power-law index of the grain size distribution of -3.5, where the grain composition is summarized in Table 1 in Birnstiel et al. (2018). In our parameter search the Beckwith and DSHARP opacity were mostly used, but OH5 and Semenov opacities were also attempted (Figure 3). OH5 is the dust opacity taken from Table 1 column 5 in Ossenkopf & Henning (1994). The dust model corresponds to grains that have coagu-

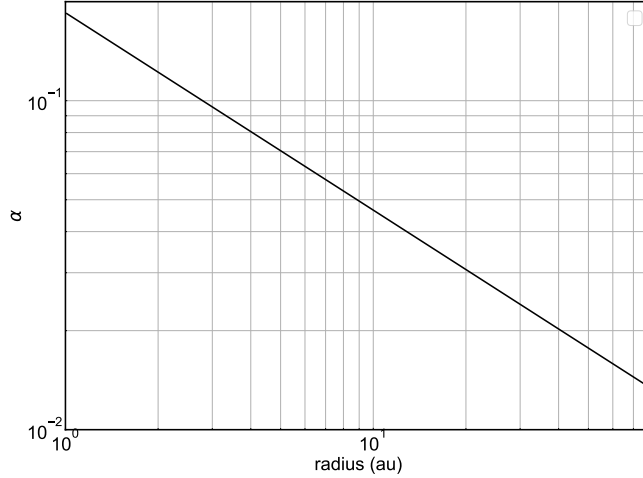


Figure 5. Radial Distribution of the α parameter in the disk of the fiducial model.

lated at a gas density of 10^6 cm^{-3} with thin ice mantles from the initial MRN distribution (Mathis et al. 1977; Draine & Lee 1984). This has been long used as a “standard” opacity table for radiative transfer models and mass estimates for embedded protostars. Regarding the Semenov opacity, the dust opacity table from Semenov et al. (2003) for the composite aggregate dust of the normal silicate mineralogy at $T < 155 \text{ K}$ is adopted.

In addition to the heating from the central protostar, we also incorporate the viscous accretion heating in the disk. The energy dissipation rate in the viscous Keplerian disk can be expressed as

$$q_{\text{heat}} = \frac{9}{4} \rho \nu_{\text{vis}} \Omega_K^2, \quad (17)$$

where ν_{vis} denotes the viscosity (Pringle 1981; D’Alessio et al. 1998). Assuming the constant ν_{vis} along the disk vertical direction and the steady accretion, the mass accretion rate \dot{M} is

$$\dot{M} = 3\pi \Sigma \nu_{\text{vis}}. \quad (18)$$

Substituting eq (18) into eq (17) to remove ν_{vis} yields

$$\begin{aligned} q_{\text{heat}} &= \frac{9}{4} \rho \Omega_K^2 \frac{\dot{M}}{3\pi \Sigma} \\ &= \frac{3\dot{M} \Omega_K^2 \rho(R, z)}{4\pi \Sigma(R)}. \end{aligned} \quad (19)$$

\dot{M} is set to be the same as that of the outer protostellar envelope. The α parameter can also be derived as

$$\alpha(R) = \frac{\nu_{\text{vis}}}{c_s h} = \frac{\dot{M}}{3\pi \Omega_K(R) h(R)^2 \Sigma(R)}. \quad (20)$$

Figure 4 shows the spatial distribution of the heating rate by the viscous accretion heating of the fiducial model. Figure 5 shows the radial profile of the α parameter in the fiducial model. The profile becomes a simple power-law with the power-law index of -0.6. The α value of ~ 0.01 -0.1 is physically reasonable for a relatively young disk (e.g., Hu et al. 2022).

With the above setting, thermal Monte Carlo simulations are performed to calculate the spatial distributions of the dust temperature. To increase the computational speed, the “modified random walk mode” implemented in RADMC-3D is adopted, and the computation is performed in parallel with 30 threads. Then radiative transfer calculations to generate the model 1.3-mm dust continuum images are made. For simplicity, we do not incorporate dust scattering in the radiative transfer calculations. Dust scattering suppresses the observed intensities (Yang et al. 2016, 2017; Yang & Li 2020; Lin et al. 2020, 2022, 2023a), while our model needs to explain the observed high brightness temperature of the 1.3-mm dust-continuum emission. Thus, inclusion of dust scattering does not change our conclusion that a dust disk passively heated by the central protostar solely cannot reproduce the observed brightness temperature.

On the assumption of equal dust and gas temperatures, radiative transfer calculations to generate the model C¹⁸O (2–1) image cubes are also conducted. The LVG mode of RADMC-3D (*i.e.*, `linemode=2`) is adopted to calculate the non-LTE population distributions of C¹⁸O, on the assumption of the maximum photon escape length of 10 au. The C¹⁸O rotational energy levels, transition frequencies, Einstein A-coefficients, and collisional coefficients with the ortho and para H₂ are

taken from the Leiden Atomic and Molecular Database (LAMDA; Schöier et al. 2005).

After the radiative transfer calculations are completed, observing simulations are conducted to directly compare the model and observed images. The CASA task *ft* was used to sample the model images with the observed *uv* coverages of the IRS 7B data, and then the CASA task *tclean* was used to make the model images with the same imaging parameters as those used for the real observational data. In the case of the C¹⁸O model, the sampled model visibility was continuum-subtracted with the CASA task *uvcontsub*, and then *tclean* was used to generate the line image cubes. Details of the imaging of the eDisk data are given by Ohashi et al. (2023).

2.4. Parameter Search

Our model requires a number of parameters and ALMA observing simulations, and thus substantial computational time. In addition, there is a possible offset of the peak position toward the southeast (Figure 1). The offset of the strong peak prevents us from calculating the numerical measure of the goodness of our axisymmetric model. Therefore, we do not adopt a numerical procedure to fit the model to the observed image such as MCMC. Instead, we searched for model parameters which decently reproduce the observed images by eye. Comparisons between the models and observations were only performed on the image plane. This is because the image-based comparison is more intuitive, and the presence of the binary companion (IRS 7B-b) complicates the modeling of visibilities. To reduce the dimension of the parameter space, limited searching parameters, which we consider directly affect the images and intensities, are chosen. Those include the disk mass (M_d), gas and dust disk radii (r_{gas} and r_{dust}), disk flaring index q , mass accretion rate (\dot{M}), disk inclination angle (i), protostellar luminosity (L_\star), and the dust mass opacity table. On the other hand, parameters such as the source distance, disk position angle, and the coordinates and wavelength of the observations are known a priori, and those parameters are fixed. Other fixed parameters are assumed to have canonical values often used in the literatures, or determined by the small preparatory parameter search (such as the protostellar mass $M_\star = 2.9 M_\odot$). The fixed parameters of the model are summarized in Table 1.

For the dust opacity table of Beckwith and DSHARP, we first tried to reproduce the extent and the aspect ratio of the observed image in the 1.3-mm dust continuum emission, and to adjust r_{dust} , M_d , and the inclination angle. Next we reproduced the peak intensity of the

continuum emission by adjusting \dot{M} and M_d . We then checked that our choice of the power law index of the radial surface density profile ($p = -0.5$) gives a decent radial intensity profile along the major axis. Next we attempted to reproduce the observed skewed intensity profile along the minor axis. We found that the disk flaring index q and M_d most affect this. As we will discuss below, q and M_d are degenerate to reproduce the asymmetric intensity profile along the minor axis, and it is not straightforward to pinpoint the best set of these two parameters. We adopt $M_d = 0.41 M_\odot$ and $q = 0.3$, both of which appears to be reasonable, as fiducial values. For the dust opacity table of OH5 and Semenov, only a small parameter search around the fiducial values were performed. These additional searches have revealed that the choice of the dust opacity table does not significantly affect the model 1.3-mm images.

Finally, with the given model image of the dust-continuum emission, we tried to reproduce the observed C¹⁸O image cube by changing r_{gas} . Here, we attempted several values of the enhanced gas-to-dust mass ratio between r_{dust} and r_{gas} and determined the fixed value of the gas-to-dust mass ratio of 5000. The factor of 50 enhancement of the gas-to-dust mass ratio was chosen to keep the dust temperature distribution flat. If the amount of the dust is further reduced, the dust temperature in that region increases. To verify the larger r_{gas} than r_{dust} , we also changed r_{dust} and checked the resultant model C¹⁸O image cubes.

Our fiducial model is model 61 in Table 2, where the disk flaring index $q = 0.30$, gas+dust disk mass $M_d = 0.41 M_\odot$, dust disk radius $r_{dust} = 62$ au, gas disk radius $r_{gas} = 80$ au, mass accretion rate $\dot{M} = 1.4 \times 10^{-6} M_\odot \text{ yr}^{-1}$, disk inclination $i = -70^\circ$, the central stellar luminosity $L_\star = 5.2 L_\odot$, and the DSHARP opacity are adopted. After the fiducial model parameters have been obtained, we changed one of the parameters to see the dependence of that particular parameter, and those parameters include L_\star , M_d , q , and \dot{M} , i.e., inclusion or exclusion of the viscous accretion heating. All the varied model parameters are listed in Table 2 in Appendix.

3. MODELING OF THE 1.3-MM DUST-CONTINUUM IMAGE

3.1. 1.3-mm Dust-Continuum Intensity

We first aim to reproduce the observed bright 1.3-mm intensity in the protostellar disk around IRS 7B-a. Figure 6 shows the model 1.3-mm dust-continuum images with and without the viscous accretion heating using the DSHARP opacity, and those without the viscous heating

Table 1. Fixed Parameters for the IRS 7B-a modeling

Parameter	Value
Radial Range	1 au – 20000 au
Distance	152 pc
Mass of the Protostar M_*	$2.9 M_\odot$
Radius of the Protostar R_*	$1.0 R_\odot$
Disk Position Angle θ_d	115°
Power Law Index of the Disk Surface Density p	- 0.5
Temperature at 1 au	400 K
Envelope Flattening Factor η_f	2.0
Radial Range of the Static Cocoon	10000 au – 20000 au
Gas Density of the Static Cocoon $n_{\text{H}_2}^{\text{coc}}$	10^4 cm^{-3}
Turbulent Velocity Dispersion in the Disk σ_{disk}	0.0 km s^{-1}
Turbulent Velocity Dispersion in the Envelope and Cocoon σ_{env}	0.2 km s^{-1}
Dust Continuum Wavelength	1.34 mm
C^{18}O Abundance $X_{\text{C}^{18}\text{O}}^{\text{can}}$	1.76×10^{-7}
Gas to Dust Mass Ratio ($r < r_{\text{dust}}, r_{\text{gas}} < r$)	100
Gas to Dust Mass Ratio ($r_{\text{dust}} < r < r_{\text{gas}}$)	5000
Ortho-to-Para Ratio of H_2	3.0
Photon Escaping Spatial Scale	10 au
Number of photons	1.5×10^6

using the other three opacities. Comparison of the observed and model intensity profiles along the major axis with the DSHARP opacity is shown in Figure 7. Without internal heating, the peak intensity of the 1.3-mm dust-continuum emission is only \lesssim half of the observed intensity, regardless of the adopted opacity (Figure 6c and Figure 7b). Incorporation of the viscous accretion heating raises the model intensities and reproduces the observed intensities (Figure 6b and Figure 7a). This is the case for all the opacity tables.

We tried to reproduce the observed 1.3-mm intensity with only the passive heating from the central protostar, adopting very high protostellar luminosities of $L_* = 20 L_\odot$ (Model 27 in Table 2), $26 L_\odot$ (Model 49), and $52 L_\odot$ (Model 60). We found that the central luminosity of $52 L_\odot$ is required to reproduce the disk brightness. This luminosity is, however, one order of magnitude higher than the measured bolometric luminosity. Even if the uncertainty of the L_{bol} measurement is taken into account, this luminosity is still a factor of \sim seven higher than the possible highest value of L_{bol} (see Section 2.3). We also changed the disk mass and dust mass opacity and checked how the model 1.3-mm dust continuum intensity changes with these parameters (see Table 2). Note that the disk mass and the dust mass opacity at the observed wavelength $\kappa_{1.3\text{mm}}$ are degenerate in con-

trolling the 1.3-mm intensity. We found that increasing M_d to $0.55 M_\odot$ does not increase the model 1.3-mm intensity (model 34). Adopting the different dust opacities seldom changes the 1.3-mm intensity (Figure 6c). This indicates that the model 1.3-mm dust-continuum emission in the protostellar disk is optically thick. Thus, the only remaining way to raise the continuum intensity is to increase the dust temperature in the disk. Figures 8 and 9 show the temperature distributions of the models with and without viscous heating, which correspond to Figure 6b and c with the DSHARP opacity. It is clear that incorporation of the viscous accretion heating raises the midplane dust temperature in the inner $\lesssim 50$ au, which enhances the dust emission intensities.

We conclude that the observed bright 1.3-mm intensity in the protostellar disk around IRS 7B-a cannot be reproduced with passive heating from the central protostar only. In other words, the protostellar disk is “self-luminous”.

3.2. Asymmetry along the Minor Axis

As well as the 1.3-mm dust-continuum intensity, the observed skewed distribution along the minor axis should be reproduced. Figure 10 shows model images (top) and intensity profiles along the disk minor axis (bottom) with different disk flaring indices q . All other model parameters are set to the fiducial values. The

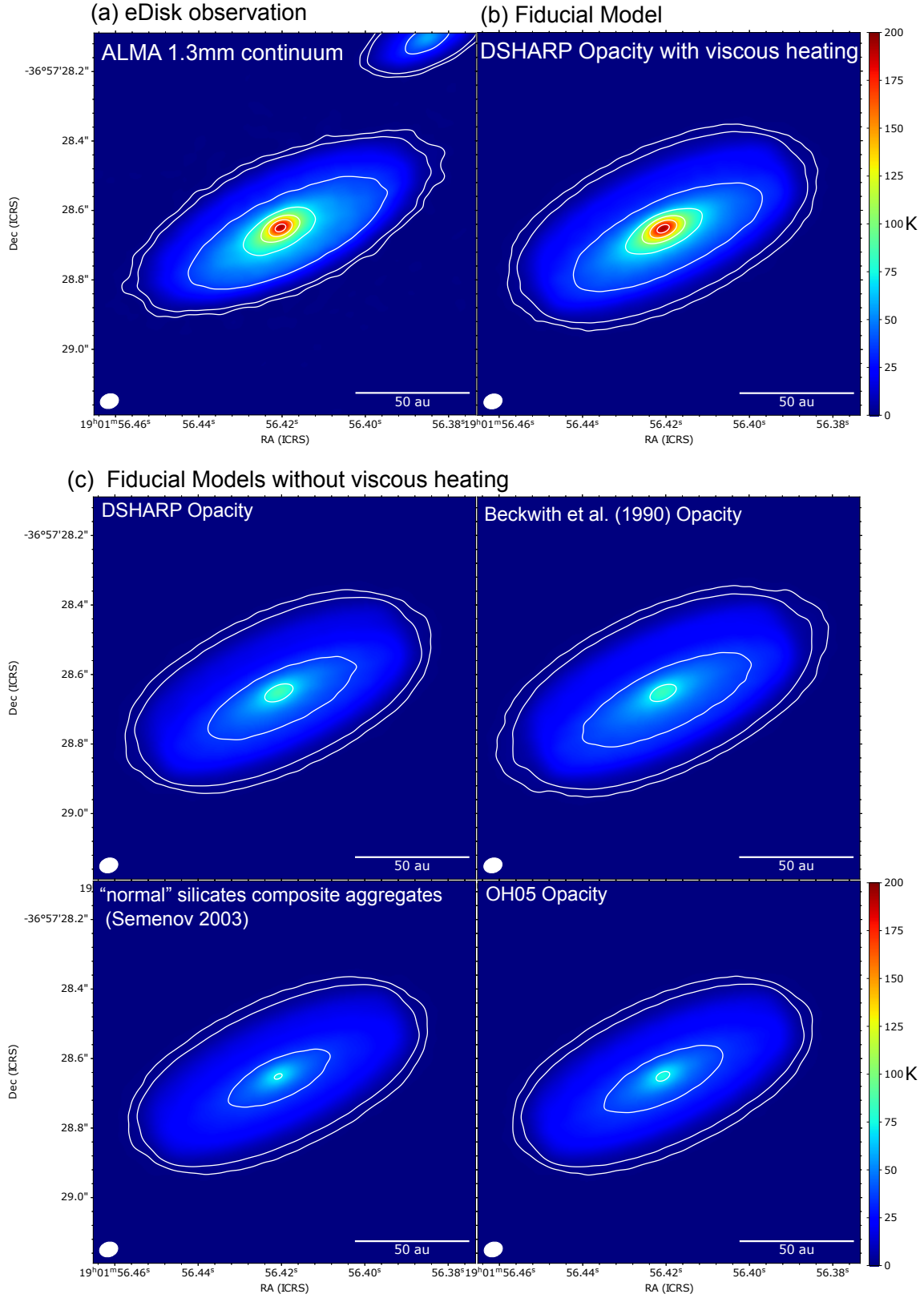


Figure 6. Comparison of the observed 1.3-mm dust-continuum image (a) to the model images with (b) or without the viscous accretion heating (c). Contour levels are the same as those in Figure 1. The model image with the viscous accretion heating adopts the DSHARP opacity and the mass accretion rate of $\dot{M} = 1.4 \times 10^{-6} M_{\odot} \text{ yr}^{-1}$, while the model images without the heating adopt four different dust opacities as labeled. Panel (b) corresponds to model 61 in Table 2, and the four models in Panel (c) correspond to models 66, 68, 69, and 70, respectively.

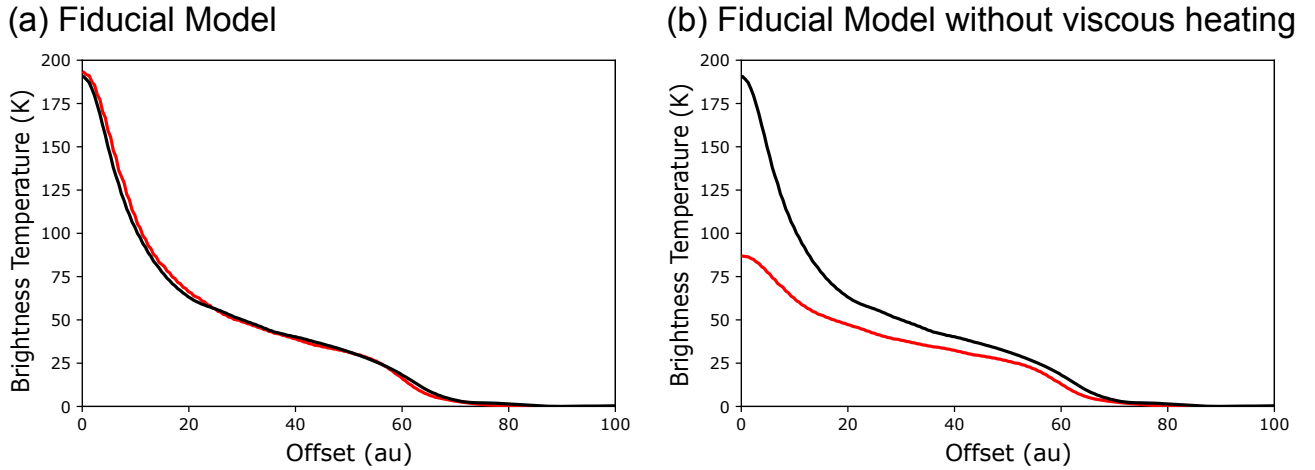


Figure 7. Comparison of the observed and model intensity profiles of the 1.3-mm dust-continuum emission. Black curves in both panels (a) and (b) show the observed intensity profile averaged in the northwest and southeast directions along the major axis. Red curves in panels (a) and (b) present the model intensity profiles with (model 61 in Table 2) and without (model 66) the viscous accretion heating, respectively.

flaring index q is defined in eq. (5). $q = 0$ indicates that the dust scale height increases linearly with r . $q = 0.25$ corresponds to the disk midplane temperature being $\propto r^{-0.5}$ and the disk being in the vertical hydro-equilibrium. In the case of $q = 0$, the model image exhibits a fairly symmetric feature (Figure 10a). The model intensity profile along the minor axis (red curve) shows little deviation from the symmetry. On the other hand, the observed intensity profile (black) shows a clear asymmetry, and there is a shallow shoulder to the southwest. If a steeper flaring index is adopted, the model images and intensity profiles exhibit more skewness along the minor axis. $q = 0.25$ reproduces the northeastern part of the observed intensity profile fairly well, while that index appears to be not enough to reproduce the southwestern shoulder (Figure 10b). In the case of $q = 0.30$ the southwestern shoulder appears to be better reproduced, while there is a small deviation to the northeastern part (Figure 10c). If an even steeper flaring index is adopted (Figure 10d), the southwestern shoulder becomes too shallow.

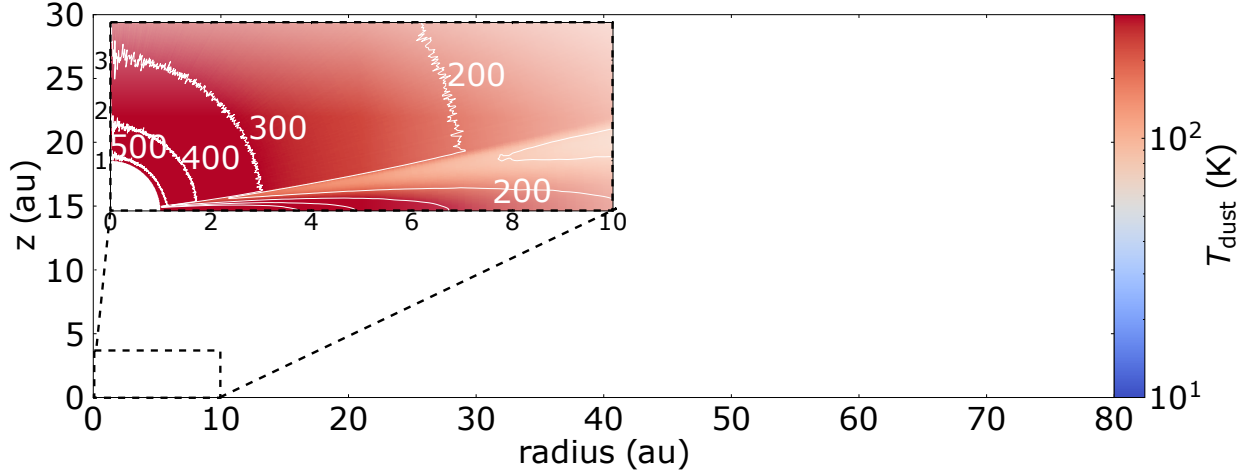
We found that if archetypal disk models with a flaring of $\frac{h}{r} \propto r^{0.25}$ and a mass of $\lesssim 0.1 M_*$ are adopted, the model image exhibits a fairly symmetric intensity profile along the minor axis (models 12-18). It is necessary to raise the disk mass to $\sim 0.41 M_\odot \approx 0.14 M_*$ to reproduce the observed asymmetry along the minor axis. On the other hand, a very high disk flaring $q \gtrsim 0.5$ is required to reproduce the asymmetry with a low disk mass (models 96 – 99). We found that either a higher flaring index or a higher disk mass is required and that the flaring index and the disk mass are degenerate, to produce the

skewed emission distribution. As fiducial values $q = 0.3$ and $M_{\text{disk}} = 0.41 M_\odot$ are adopted.

Figure 11 presents a schematic figure to explain the cause of the asymmetry along the minor axis. We consider the line of sights (LOSs) B and C offset from the LOS toward the disk center (LOS A). Even though the amount of the offset of those LOSs from the center are the same on the upper and lower sides in Figure 11, those on the lower side directly see the hot disk surface if the dust-continuum emission there is optically thick. On the other hand, on the upper side, the LOSs encounter the colder midplane regions. Thus, the overall emission distribution should be skewed to the lower side. If the LOSs are far from the disk center (LOS D), those portions become optically thin. Thus, at larger radii, the asymmetric distribution becomes less significant. These portions correspond to the elliptical region as denoted by a dashed line in Figure 1. If the disk is more inclined or more flared, the LOS toward the disk center (LOS A) passes through a portion of the flared disk in the near side. The near-side portion of the flared disk affects the observed intensity at the central LOS, and the central position can be dimmer. The extreme case is the perfectly edge-on disk in HH 212 mms, which produces a dark lane at the disk midplane and a morphology shaped as a “space hamburger” (Lee et al. 2017).

Thus, both disk flaring and optically thickness of the dust emission are required to produce the skewed emission distribution. If the disk is perfectly geometrically thin, or the dust emission is perfectly optically thin, the emission distribution should always be symmetric. The degeneracy between the flaring index and disk mass found by our modeling is naturally explained since more

(a) *Temperature Distribution with viscous heating* ($\dot{M} = 1.4 \times 10^{-6} M_{\odot} \text{ yr}^{-1}$)



(b) *Temperature Distribution without viscous heating*

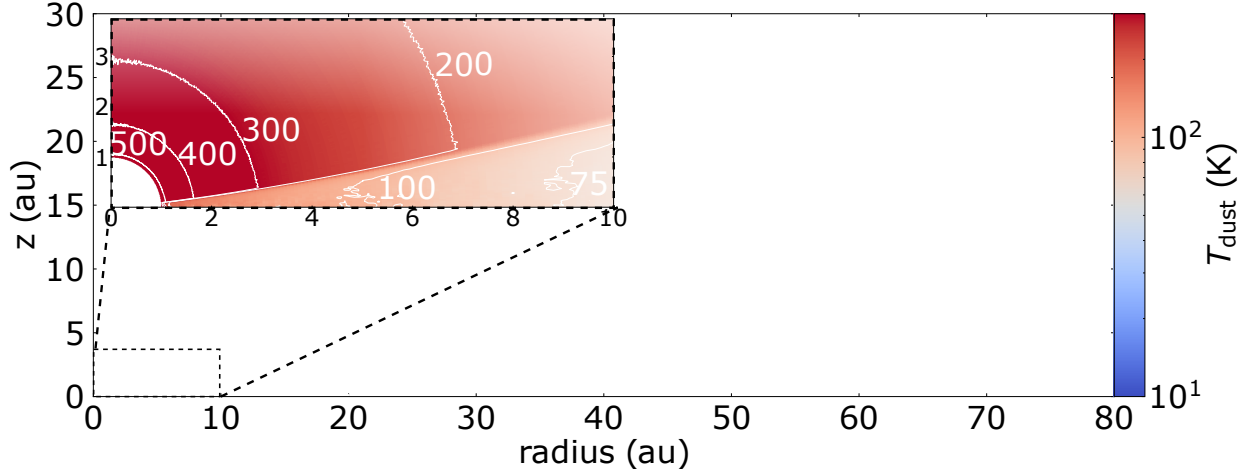


Figure 8. Distribution of the dust temperature in the disk region with (a; model 61 in Table 2) and without the viscous accretion heating (b; model 66). Contour levels are 25, 50, 75, 100, 200, 300, 400, and 500 K.

flared disks require less optical depth, and less flared disks require more optical depth. On the other hand, disk stability with a given disk mass can be evaluated with the Toomre Q value as:

$$Q = \frac{c_s \Omega_K}{\pi G \Sigma}, \quad (21)$$

where the formulae of c_s , Ω_K , and Σ are given in eqs (3), (4), (6), respectively. Note that the Q value depends on R . Adopting the fiducial disk mass of $0.41 M_{\odot}$ and the dust temperature shown in Figure 9a to calculate c_s , the Toomre Q values are calculated to be ~ 11.2 , 2.2, and 1.0 at $R = 10$, 30, and 50 au, respectively. Thus, the inner region is gravitationally stable, but the outer region can be unstable. In combination with an appropriate value of the disk flaring index of ~ 0.3 , the fiducial value of the disk mass is thus reasonable.

4. MODELING OF THE C^{18}O IMAGE CUBE

After reproducing the observed 1.3-mm dust-continuum image, we seek to reproduce the observed intensities and spatial and velocity distributions of the C^{18}O (2–1) emission next. The C^{18}O (2–1) emission has been adopted as a good probe of protostellar disks and envelopes (e.g., Ohashi et al. 2014; Yen et al. 2014; Aso et al. 2015). Black contours and colors in Figure 12 show the observed velocity channel maps of the C^{18}O (2–1) emission in IRS 7B-a (Ohashi et al. 2023). While the C^{18}O emission exhibits a velocity gradient along the disk major axis and a signature of Keplerian rotation, the molecular emission is detected only at the outskirts of the dust disk (white contours in Figure 12). This is because the molecular emission is buried in the bright dust-continuum emission (see section 5.2 for the mech-

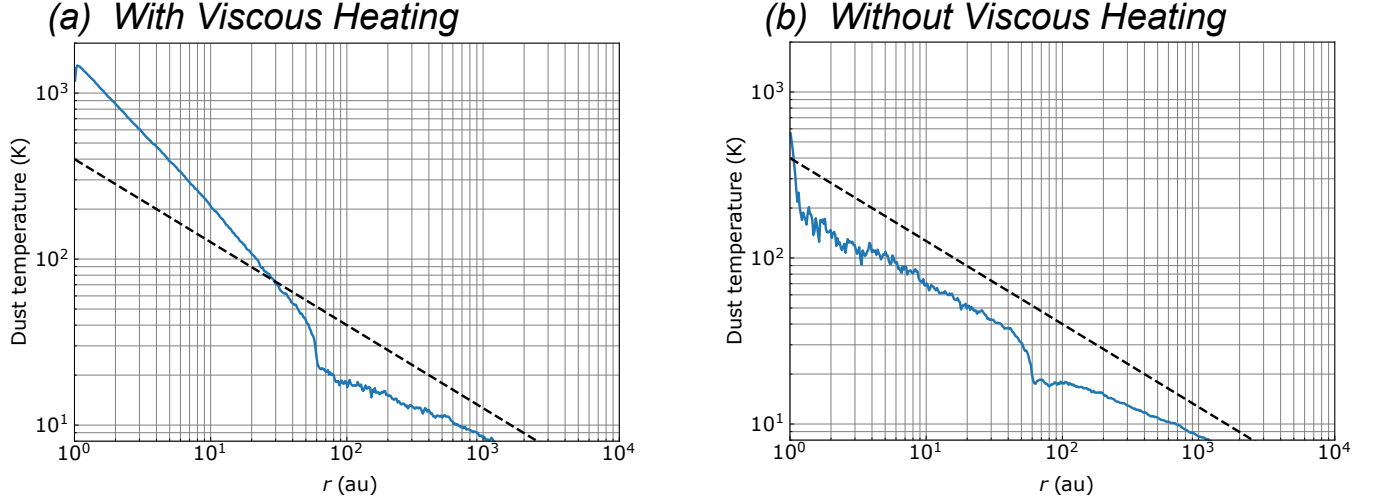


Figure 9. Radial temperature profiles (blue lines) in the disk midplane with (a; model 61 in Table 2) and without the viscous accretion heating (b; model 66). Dashed lines show the temperature profile of $400 \text{ (K)} \times (r/1 \text{ au})^{-0.5}$.

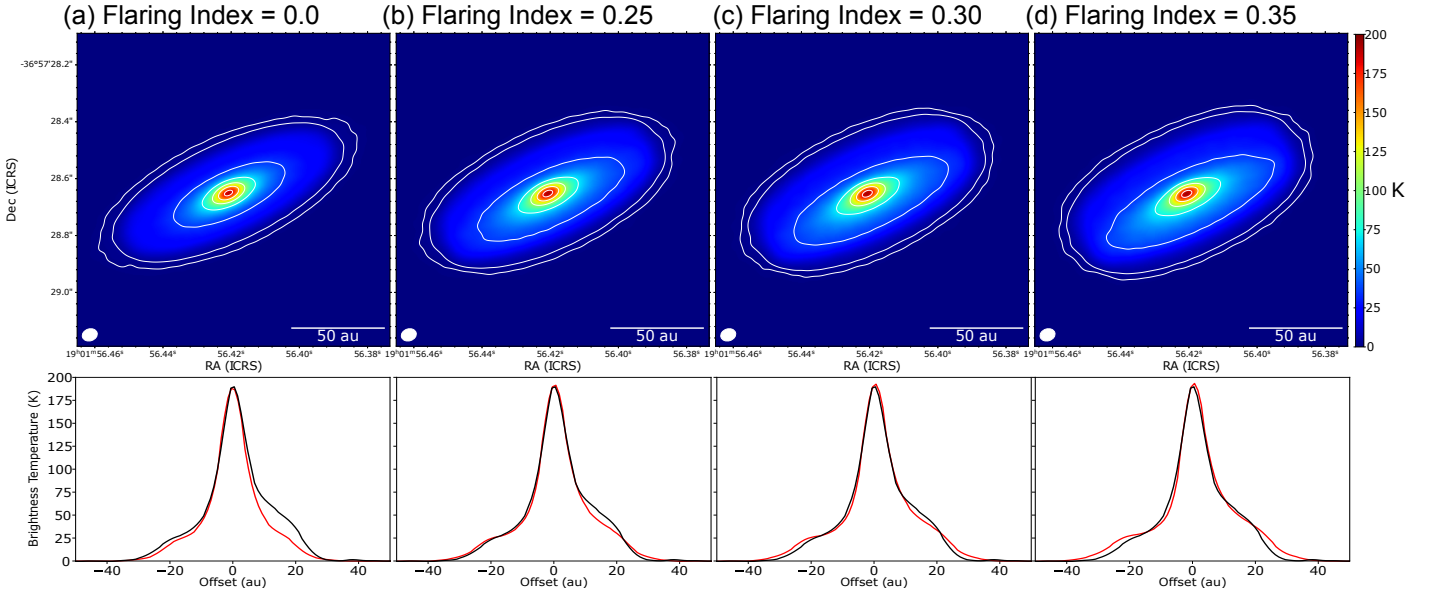


Figure 10. Upper panels: Model 1.3-mm dust-continuum images with different flaring indices of the dust distribution as labeled. Contour levels are the same as those in Figure 1. Lower panels: Relevant intensity distributions along the minor axis (red curves) to be compared to the observed intensity profile (black). Panels (a), (b), (c), and (d) correspond to models 4, 28, 61 (Fiducial), and 85, respectively, in Table 2.

anism of the absence of the molecular emission toward the dust-continuum emission).

In our modeling of the C^{18}O emission we first adopted the same radius of the gas disk as that of the dust disk (e.g., $r_{\text{gas}}=r_{\text{dust}}=62 \text{ au}$ in model 74 and $r_{\text{gas}}=r_{\text{dust}}=80 \text{ au}$ in model 76; see Table 2). In these cases, however, the C^{18}O emission is significantly suppressed, and the observed C^{18}O emission cannot be reproduced. We found that a larger radius of the gas disk is required to reproduce the observed inten-

sities as well as the spatial and velocity distributions of the C^{18}O emission (fiducial model 61). As both the $r_{\text{gas}}=r_{\text{dust}}=62 \text{ au}$ and $r_{\text{gas}}=r_{\text{dust}}=80 \text{ au}$ cases yield the significantly suppressed C^{18}O emission, the difference of the gas and dust radii is unlikely to be due to the effect of the noise in the continuum data.

To ensure the difference of the gas and dust radii, the CASA observing simulator including the noise is applied to the calculated C^{18}O model image cubes. Note that the signal-to-noise ratio of the continuum emission is

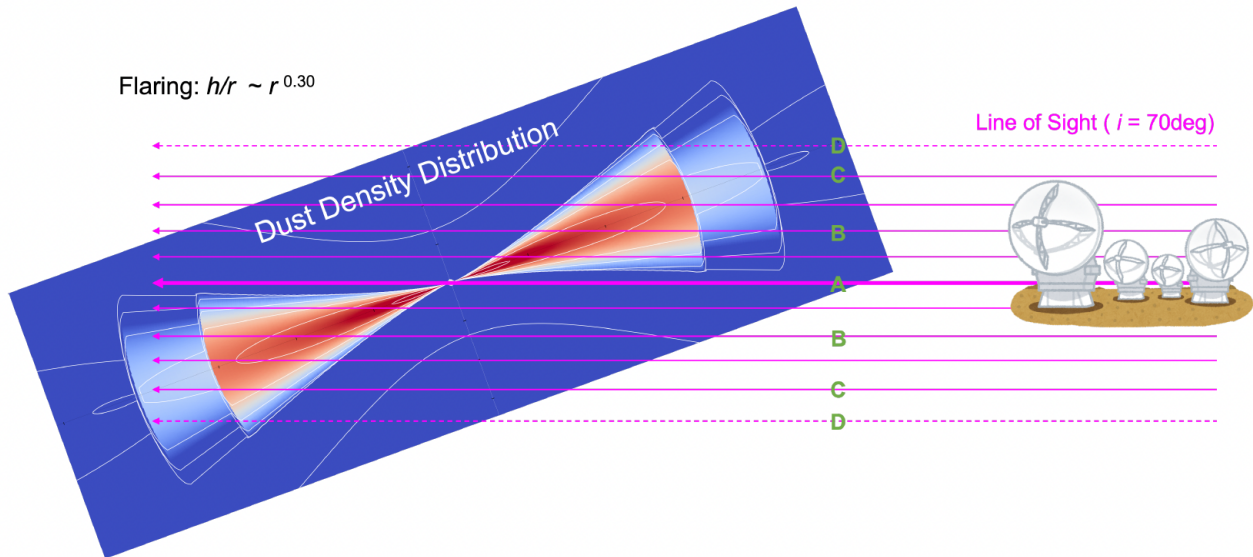


Figure 11. Schematic picture to interpret the skewed distribution of the 1.3-mm dust-continuum emission along the minor axis. The dust distribution in the model disk, inclined by 70° to the line of sight of the observer, is shown. Line of sights toward the center (A) and the offset positions (B,C,D) are drawn. Contour levels and color scale are the same as those in Figure 2c.

higher than or comparable to that of the $C^{18}O$ emission in the $C^{18}O$ emission region (see Figure 12). Two model image cubes, one with $r_{gas}=80$ au and $r_{dust}=62$ au (fiducial) and the other with $r_{gas}=r_{dust}=62$ au are adopted for the CASA simulations. Note that these two models do not adopt the CASA task *ft* but *simobserve* to include the noise (models 100 and 101, respectively). The model velocity channel maps of the $C^{18}O$ emission with the gas disk radius of 80 au (model 100) are overlaid in Figure 12 (red contours). The overall locations of the $C^{18}O$ emission, shapes, and intensities are broadly reproduced with the model. Figure 13a compares the observed and model PV diagrams along the major axis of the dust disk. The observed emission location in the PV diagram is reproduced with the model. In contrast, the model with the gas radius identical to the dust radius (model 101) cannot reproduce the observed intensities (Figure 13b). These results suggest that the radius of the gas disk is larger than that of the dust disk in IRS 7B-a.

5. DISCUSSION

5.1. Self-Luminous Protostellar Disks

Our modeling and parameter search have found that models of dusty disks only passively heated by the central protostar cannot reproduce the observed bright 1.3-mm dust-continuum intensities. The observed peak brightness temperature is as high as ~ 195 K. To reproduce such a high dust brightness temperature, internal heating by the viscous accretion, along with the optically thick dust emission, is incorporated. Then, with a typ-

ical mass accretion rate of $\sim a \text{ few } \times 10^{-6} M_\odot \text{ yr}^{-1}$ the observed brightness temperature in the disk can be reproduced. In other words, the inner part of the IRS 7B-a disk is self-luminous, with most of the heating coming from the release of gravitational energy as the material in the disk spirals inward gradually as it loses angular momentum.

Such a high peak brightness temperature of the 1.3-mm dust continuum emission in IRS 7B-a is not unique but seen in several other eDisk targets, such as IRAS 04166+2706 (133 K), BHR 71 IRS1 (170 K), Oph IRS 63 (170 K), R CrA IRAS 32A (153 K), and TMC-1A (187 K) (Ohashi et al. 2023). While a modeling effort tailored for these targets is required, these high brightness temperatures likely suggest that these protostellar disks are also self-luminous. In contrast, among the 20 sources in the DSHARP sample, no source shows the peak brightness temperature of the 1.3-mm dust-continuum emission higher than 150 K, and most sources show the peak brightness temperatures lower than ~ 60 K (Andrews et al. 2018). Peak 1.3-mm brightness temperatures of edge-on Class II disks are even lower (5-10 K; Villenave et al. 2020). These results suggest a systematic difference of the physical conditions between the protostellar and protoplanetary disks.

Alarcón et al. (2023) constructed detailed models of the dust disk around V883 Ori, a Class I FU-Ori object, which has been studied as an intriguing astrochemical laboratory (van 't Hoff et al. 2018; Tobin et al. 2023). Their model also demonstrates that the viscous accretion heating is required to reproduce the observed high

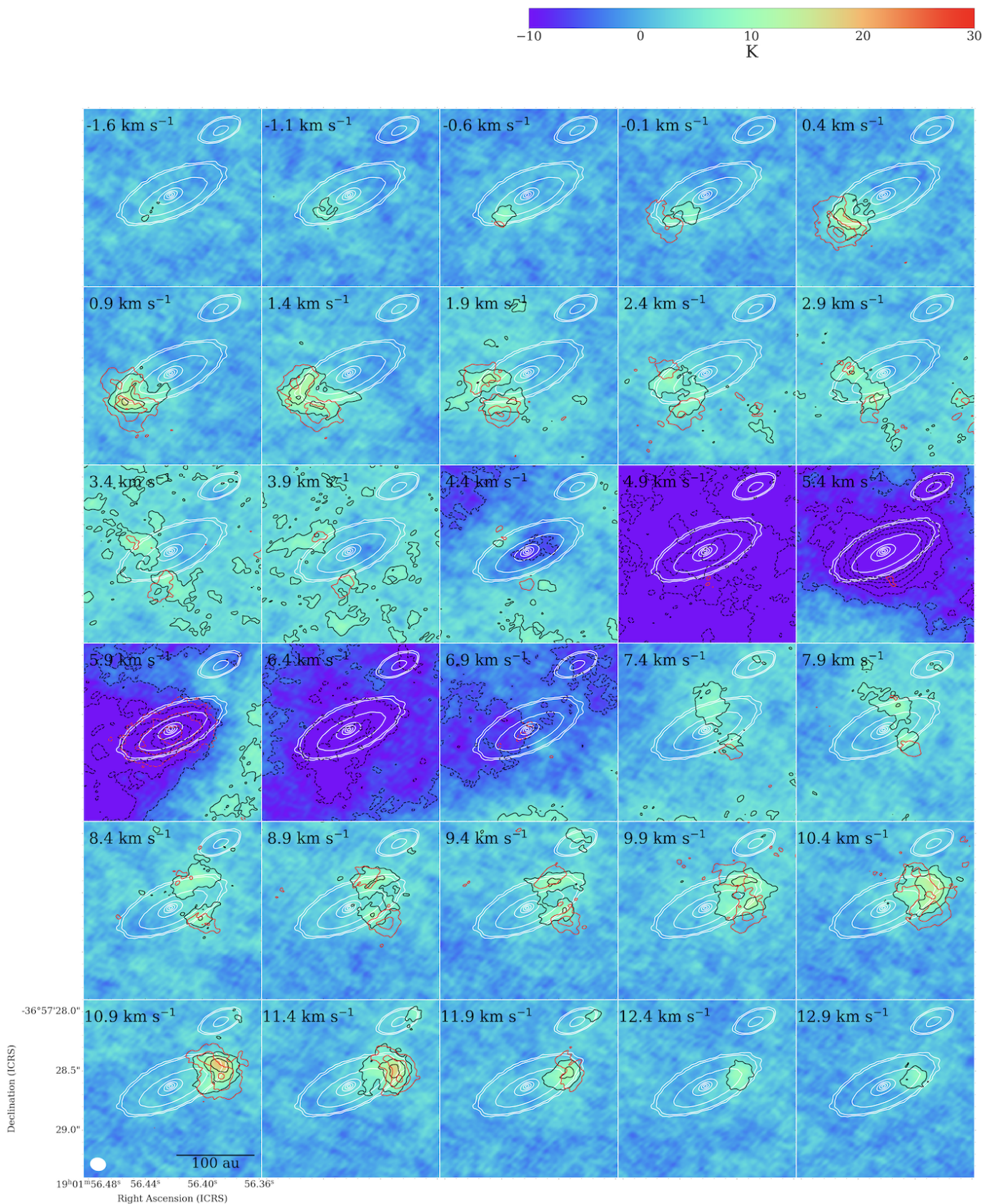


Figure 12. Comparison of the observed (black contours and colors) and model C^{18}O (2–1) velocity channel maps (red) in IRS 7B-a (model 61 in Table 2). Contour levels of the C^{18}O emission start from -18σ in steps of 3σ ($1\sigma = 1.72$ K). White contours show the map of the observed 1.3-mm dust-continuum emission, where the contour levels are same as those in Figure 1.

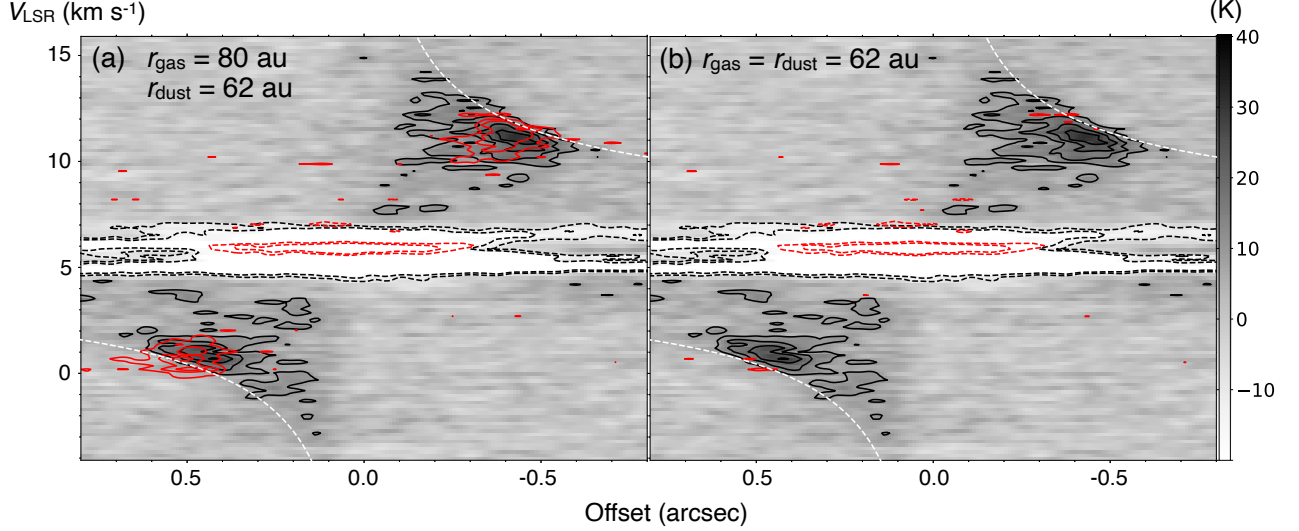


Figure 13. Comparison between the observed (black contours and grayscale) and model P-V diagrams (red contours) of the C^{18}O (2–1) emission along the major axis (P.A. = 115°). Panel (a) shows the model P-V diagram with a dust radius of 62 au and a gas radius of 80 au including the noise (model 100 in Table 2), while Panel (b) with the gas and dust radius of 62 au including the noise (model 101). Contour levels are -5σ , -3σ , 3σ , 5σ , 7σ , 9σ , and 11σ ($1\sigma = 2.98$ K). White dashed curves denote the Keplerian rotation curve with a central protostellar mass of $2.9 M_\odot$ and a disk inclination angle $i = 70^\circ$.

(~ 500 K) brightness temperature of the 1.3-mm dust-continuum emission. The presence of viscous accretion heating in protostellar disks has also been suggested in other variable sources (Contreras Peña et al. 2020; Yoon et al. 2021) and a massive protostar GGD 27-MM1 (Añez-López et al. 2020). While IRS 7B appears to be more quiescent than V883 Ori, our modeling also proves that even in the quiescent phase the viscous accretion heating is required to reproduce the dust brightness.

5.2. Coupling between Dust and Molecular-Line Emission

In this subsection, we argue that the observed high brightness temperatures of the dust emission affect the interpretation of the molecular line images. We here consider two simple cases (see Bosman et al. 2021). One is that the dust and gas are located in separate layers (e.g., disk and envelope, respectively), and that the optically-thick dust emission resides behind the foreground molecular emission. In such a case, the observed brightness temperature of the molecular line ($\equiv T_B^{mol}$) is expressed as,

$$T_B^{mol} = (J_\nu(T_{\text{ex}}) - J_\nu(T_{\text{dust}}))(1 - \exp(-\tau_{\nu,\text{gas}})), \quad (22)$$

where

$$J_\nu(T) = \frac{\frac{h_P \nu}{k_B}}{1 - \exp(\frac{h_P \nu}{k_B T})}. \quad (23)$$

In the above expressions, ν is the line frequency, h_P is Planck constant, T_{ex} is the excitation temperature of

the molecular line, and T_{dust} is the dust temperature. $\tau_{\nu,\text{gas}}$ is the optical depth of the molecular line. If T_{ex} is close to T_{dust} , T_B^{mol} is close to zero, no matter what the value of $\tau_{\nu,\text{gas}}$ or the molecular column density is. If T_{ex} is lower than T_{dust} , the line shows an absorption.

The other case is that both dust and gas are in the same space with the same volume. T_B^{mol} is expressed as:

$$\begin{aligned} T_B^{mol} &= J_\nu(T)(1 - \exp(-(\tau_{\nu,\text{dust}} + \tau_{\nu,\text{gas}}))) \\ &\quad - J_\nu(T)(1 - \exp(-\tau_{\nu,\text{dust}})) \\ &= J_\nu(T) \exp(-\tau_{\nu,\text{dust}})(1 - \exp(-\tau_{\nu,\text{gas}})). \end{aligned} \quad (24)$$

Here we assume $T_{\text{ex}} = T_{\text{dust}} = T$. In this case, if $\tau_{\nu,\text{dust}} \gg \tau_{\nu,\text{gas}}$, T_B^{mol} is close to zero. Note that the absolute value of the dust optical depth does not matter. In the case of $\tau_{\nu,\text{dust}} \gg \tau_{\nu,\text{gas}}$, T_B^{mol} is always very low even if $\tau_{\nu,\text{dust}} < 1$.

The depression or even absorption of the molecular line emission toward the continuum emission is commonly seen in ALMA observations of protostellar sources, including our eDisk observations (van't Hoff et al. 2023; Lin et al. 2023b). These phenomena are often referred to as “continuum over-subtraction.” From the considerations above, a possible reason for the absence of the molecular line emission toward the continuum emission is either line excitation temperatures close to or lower than the dust temperatures, or the dust optical depth higher than the line optical depth, or combination of both. Both high dust temperature and high dust optical depth produce high observed dust bright-

ness temperatures. In the case of protostellar sources, molecular emission are originated not only from the protostellar disk but also from the protostellar envelope. At lower velocities, the molecular emission from the disk is blended with that from the colder envelope. Such envelope blending induces suppression or absorption of the molecular line toward the bright dust disk. The observed velocity channel maps indeed show that around the systemic velocity ($V_{\text{LSR}} = 4.90\text{-}6.40 \text{ km s}^{-1}$), there is no observed line emission but a strong absorption feature (Figure 12). The C^{18}O model does not predict any emission in this velocity range. While the line width of the absorption feature is narrower, the C^{18}O model also reproduces the absorption feature at $V_{\text{LSR}} = 5.9 \text{ km s}^{-1}$ as shown in dashed red contours in Figure 12.

To trace gas structures, kinematics and chemistry in the inner parts of dusty disks, molecular lines which are optically thicker than the dust emission are required. On the other hand, if the optical depth of that molecular line is too high, the molecular line cannot trace the disk internal structures (Liu et al. 2018). In the case of embedded sources, optically-thick molecular lines trace only the cold outer envelopes, which results in the absorption against the bright continuum emission originated from the disk. It is not straightforward to identify appropriate molecular tracers for protostellar disks. Different degrees of the missing flux between the continuum and line images in interferometric observations also complicate the interpretation of the observed images. If the original line + continuum image is totally uniform because of the optically-thick line emission, the line + continuum image after the interferometric observations is severely suppressed. After the continuum subtraction, the line only image shows the negative signal at the continuum position.

It is important to recall that our model assumes a constant C^{18}O abundance and gas-to-dust mass ratio in the disk and envelope, except for the outer dust-free region in the disk (Figure 2). Our modeling demonstrates that even in such a case the C^{18}O emission is suppressed in the disk. The observed image could be misunderstood as the CO depletion in the disk. The same warning applies to the analysis of other lines. Detailed radiative transfer modeling coupled with the interferometric observing simulations is required to interpret the interferometric images correctly and to quantitatively study the physical and chemical conditions of protostellar disks.

5.3. Dust Distribution in the Protostellar Disk

Our modeling also found that the observed skewness of the 1.3-mm dust-continuum emission along the disk minor axis can be reproduced with the flared disk model

and that the dust emission is optically thick. Dust in the protostellar disk is yet to be settled. Such asymmetric distributions of the 1.3-mm dust continuum emission along the disk minor axes are also observed in other eDisk targets, including CB 68 (Kido et al. 2023), L1527 IRS (van't Hoff et al. 2023), IRAS 04302+2247 (Lin et al. 2023b), and GSS30 IRS 3 (Santamaría-Miranda et al. 2023), as well as the space hamburger in HH212 mms (Lee et al. 2017). These results suggest that at least in several of the protostellar disks the dust vertical distributions are flared (Ohashi et al. 2023).

The above result is in sharp contrast to the observed geometrically thin dust distributions in protoplanetary disks around Class II sources. Concentric ring/gap features are commonly seen in such Class II disks. If the dust distributions are flared vertically and the disk rotational axes are inclined with respect to the LOS, such ring/gap features can easily be hidden by the geometrical effect. Thus, the dust is already settled in such more evolved disks (Pinte et al. 2016). The 1.3-mm dust-continuum images of highly inclined ($i \gtrsim 70^\circ$) Class II disks also show ring/gap features, which strongly implies that the dust distribution is geometrically thin (Villenave et al. 2020, 2022). Among the eDisk targets, two of the most evolved sources, L1489 IRS and Oph IRS63, show signatures of concentric rings/gaps in the disks (Ohashi et al. 2023; Yamato et al. 2023; Flores et al. 2023). These disks do not show asymmetry along the disk minor axes. Dust settling and formation of ring/gap features in the disks are thought to likely proceed between the Class I to Class II stages, as also discussed in Ohashi et al. (2023).

On the other hand, our combined dust continuum and C^{18}O modeling has also revealed that the radius of the gas disk ($\sim 80 \text{ au}$) should be larger than that of the dust disk ($\sim 60 \text{ au}$) around the Class I protostar IRS 7B-a. In more-evolved, protoplanetary disks around Class II sources, observationally-measured radii of CO disks (*e.g.*, curves of growth) are systematically larger than the corresponding dust radii, and the gas radii are 2-2.5 times larger than the dust radii (Ansdell et al. 2018; Andrews 2020). The effect of the optical depth and radial variation of dust κ , however, complicate the interpretation of the apparent discrepancy between the gas and dust radii (Hughes et al. 2008). Trapman et al. (2019) suggest that a factor of 4 larger gas radii is required to unambiguously prove the radial drift of dust. On the other hand, simultaneous radiative transfer modeling of gas and dust disks show that the same gas and dust radii with the constant gas-to-dust ratio cannot reproduce the CO and dust intensity profiles and the difference between them (Panić et al. 2009; Andrews et al.

2012; Ansdell et al. 2018; Facchini et al. 2019). These results imply presence of dust radial drift in the Class II stage. In the case of the Class I protostar IRS 7B, we make use of the simple observational results that the molecular line is severely suppressed due to the strong dust emission in the dust disk region, and that the gas emission is only visible at the outskirts of the dust disk. To reproduce such observational images the gas disk radius larger than the dust radius should be incorporated. This implies that dust grains may have migrated radially inward with respect to the molecular gas in the Class I disk, even though they are not settled onto the disk midplane yet.

The above conclusion may seem surprising at first sight. In the simplest case of a smooth laminar disk, the time scale for radial migration of the dust relative to the gas:

$$t_{rad} \equiv \frac{R}{|v_{r,d} - v_{r,gas}|} \approx \frac{1}{\eta \tau_s \Omega_K} \quad (25)$$

is much longer than the time scale for the dust to settle vertically:

$$t_z \equiv \frac{z}{|v_{z,d}|} \approx \frac{1}{\tau_s \Omega_K} \quad (26)$$

in the small particle limit (with the dimensionless Stokes number $\tau_s \ll 1$, see Sections 7.1 and 7.2 of the review article by Armitage 2017), where R is the cylindrical radius, $v_{r,d}$ and $v_{r,gas}$ the radial velocity of the dust and gas respectively, Ω_K the local Keplerian frequency, z the vertical distance from the midplane, $v_{z,d}$ the dust settling terminal speed, and $\eta \propto (h/R)^2 \ll 1$ measures the fractional deviation of the gas rotation speed from the local Keplerian value. A potential solution to this apparent contradiction is that the dust is prevented from settling by turbulence in the disk, which may also be required to drive the relatively high mass accretion rate inferred from the dust continuum modeling. The nature of the turbulence and how it may affect the radial dust migration remain unclear and deserve further investigation. In the circumterinary dust ring around the GG Tau system, Tang et al. (2023) proposed that the angular difference of the polarization direction from the tangent of the ring could be due to the radial flow of the dust grains. The radial drift velocity estimated from the angle difference is, however, ~ 3 times faster than the theoretical prediction using the same formula by Armitage (2017).

6. SUMMARY

We have constructed a physical model that reproduces the 1.3-mm dust-continuum emission and the $C^{18}O$ (2–1) emission toward the Class I protostar R CrA IRS 7B-a, observed with our ALMA Large Program, eDisk. The

gas and dust density distributions are given, and thermal Monte Carlo simulations are performed to calculate the spatial distribution of the dust temperature with RADMC-3D. From the spatial distributions of gas and dust as well as the calculated temperature distribution, the images of the 1.3-mm dust-continuum emission and $C^{18}O$ (2–1) emission are made with RADMC-3D, followed by the observing simulations. A number of such images were created to search by eye for the model parameters that decently reproduce the intensities and the spatial and velocity distributions of the observed emissions. Our modeling effort has found the following insights into the physical properties of the protostellar disk.

1. Dust disk models passively heated by the central protostar solely cannot reproduce the observed bright intensity of the 1.3-mm continuum emission, regardless of the adopted dust mass opacity table and the disk mass. The 1.3-mm dust-continuum emission in the disk is optically thick, and a change of $\kappa_{1.3mm}$ or disk mass does not increase the 1.3 mm intensity significantly. The 1.3-mm intensity in such models is a factor $\gtrsim 2$ lower than the observed intensity. We found that the inclusion of the viscous accretion heating in the disk with a mass accretion rate of $\dot{M} \sim 10^{-6} M_\odot \text{ yr}^{-1}$ can reproduce the observed 1.3-mm intensities. Several other eDisk targets also exhibit similar high brightness temperatures of the 1.3-mm dust continuum emission originating from the disk. These results suggest that the protostellar disks are self-luminous. In contrast, disks around Class II sources do not show such high dust intensities, suggesting a difference in the physical conditions between the protostellar and Class II disks.
2. The observed asymmetry of the 1.3-mm dust continuum image along the minor axis is reproduced with a flared dust disk model, where the flaring power-law index $q \sim 0.3$ as defined by $\frac{h}{r} \sim r^q$ and the disk mass $\sim 14\%$ of the central protostellar mass. The flaring index and disk mass are degenerate in reproducing the observed skewed intensity profile along the disk minor axis. This is because the $\tau = 1$ disk surface is determined by the dust mass distribution, which in turn is set by the total dust mass and flaring parameter. Similar asymmetric structures of the dust emission along the disk minor axes are seen toward several other eDisk protostellar disks, suggesting that the dust in these protostellar disks is yet to settle to the midplane. This is different from the geometrically-

thin dust distribution in the disks around Class II sources associated with ring/gap features. These results suggest that dust settling and formation of ring/gap features in the disks proceed between the Class I and Class II stages.

3. To reproduce the observed distribution of the $C^{18}O$ emission, the radius of the gas disk should be ~ 80 au, i.e., larger than that of the dust disk radius (~ 60 au). In the models with the gas disk radius identical to the dust disk radius, the molecular emission is severely suppressed because of the obscuration by the high brightness and opacity of the dust emission.
4. Our radiative transfer model, combined with the observing simulations, reproduces the observed depression of the $C^{18}O$ emission toward the continuum emission. Around the systemic velocity, the observed absorption of the $C^{18}O$ line is also reproduced with our model. The absorption feature should be originated from the higher background dust brightness temperature than the line excitation temperature. The depression of the molecular emission is also caused by the higher dust optical depth than the line optical depth. Note that gas components are present throughout the disk, with a constant $C^{18}O$ abundance, in our models. While the apparent depressions of the molecular emission in the disks observed with ALMA are often interpreted as a real depletion of the molecule, they could be caused by radiative transfer effects, which are further enhanced by interferometric filtering. Detailed radiative transfer modeling and interferometric observing simulations are required to interpret interferometric images correctly.

We would like to thank all the ALMA staff supporting this work. S.T. is supported by JSPS KAKENHI grant Nos. JP21H00048 and JP21H04495 and by NAOJ ALMA Scientific Research grant No. 2022-20A. K.S. is supported by JSPS KAKENHI grant No. JP21H04495. N.O. acknowledges support from National Science and Technology Council (NSTC) in Taiwan through grants NSTC 109-2112-M-001-051 and 110-2112-M-001-031. J.J.T. acknowledges support from NASA RP 80NSSC22K1159. J.K.J., R.S., and S.G. acknowledge support from the Independent Research Fund Denmark (grant No. 0135-00123B). Y.A. acknowledges support by NAOJ ALMA Scientific Research Grant code 2019-13B, Grant-in-Aid for Scientific Research (S) JP18H05222, and Grant-in-Aid for Transformative Research Areas (A) JP20H05844

and JP20H05847. F.J.E. acknowledges support from NSF AST-2108794. I.D.G.-M. acknowledges support from grant PID2020-114461GB-I00, funded by MCIN/AEI/10.13039/501100011033. P.M.K. acknowledges support from NSTC 108-2112-M-001-012, NSTC 109-2112-M-001-022, and NSTC 110-2112-M-001-057. W.K. was supported by the National Research Foundation of Korea (NRF) grant funded by the Korea government (MSIT) (NRF-2021R1F1A1061794). S.-P.L. and T. J.T. acknowledge grants from the NSTC of Taiwan 106-2119-M-007-021-MY3 and 109-2112-M-007-010-MY3. C.W.L. is supported by the Basic Science Research Program through the NRF funded by the Ministry of Education, Science and Technology (NRF-2019R1A2C1010851) and by the Korea Astronomy and Space Science Institute grant funded by the Korea government (MSIT; project No. 2022-1-840-05). J.-E.L. is supported by the NRF grant funded by the Korean government (MSIT; grant No. 2021R1A2C1011718). Z.-Y.L. is supported in part by NASA NSSC20K0533 and NSF AST-2307199 and AST-1910106. Z.-Y.D.L. acknowledges support from the Jefferson Scholars Foundation, the NRAO ALMA Student Observing Support (SOS) SOSPA8-003, the Achievements Rewards for College Scientists (ARCS) Foundation Washington Chapter, the Virginia Space Grant Consortium (VSGC), and UVA research computing (RIVANNA). L.W.L. and F.J.E. acknowledge support from NSF AST-2108794. S.M. is supported by JSPS KAKENHI grant Nos. JP21J00086 and JP22K14081. S.N. acknowledges support from the National Science Foundation through the Graduate Research Fellowship Program under grant No. 2236415. P.D.S. acknowledges support from NSF AST-2001830 and NSF AST-2107784. K.T. is supported by JSPS KAKENHI grant Nos. JP21H04487, JP22KK0043, and JP21H04495. M.L.R.H. acknowledges support from the Michigan Society of Fellows. J.P.W. acknowledges support from NSF AST-2107841. Y.Y. is supported by the International Graduate Program for Excellence in Earth-Space Science (IGPEES), World-leading Innovative Graduate Study (WINGS) Program of the University of Tokyo. H.-W.Y. acknowledges support from the NSTC in Taiwan through grant NSTC 110-2628-M-001-003-MY3 and from the Academia Sinica Career Development Award (AS-CDA-111-M03). This paper makes use of the following ALMA data: ADS/JAO.ALMA #2019.1.00261.L and 2019.A.00034.S. ALMA is a partnership of ESO (representing its member states), NSF (USA), and NINS (Japan), together with NRC (Canada), NSTC and ASIAA (Taiwan), and KASI (Republic of Korea), in cooperation with the Republic of Chile. The Joint

ALMA Observatory is operated by ESO, AUI/NRAO, and NAOJ. The National Radio Astronomy Observatory is a facility of the National Science Foundation operated

under cooperative agreement by Associated Universities, Inc.

APPENDIX

A. SEARCHED MODEL PRAMETERS

Table 2 lists all the sets of the calculated model parameters, sorted by the disk flaring index q and then the disk mass M_d , except for models 100-102 which adopt *simobserve* instead of *ft*. Note that we did not attempt to cover the complete parameter space, but tried to approach to the model images which reproduce the observed images.

Table 2. Parameter Search for the IRS 7B-a modeling

Model	Grid (r, θ, ϕ)	Flaring Index, q	M_d (M_\odot)	r_{dust} (au)	r_{gas} (au)	Mass Accretion Rate \dot{M} ($\times 10^{-6} M_\odot \text{ yr}^{-1}$)	Dust Opacity	Disk inclination ($^\circ$)	Stellar Luminosity (L_\odot)
1	(512, 512, 1)	0.00	0.39	60	80	0.0	Beckwith	-70	5.2
2	(512, 512, 1)	0.00	0.39	60	80	1.9	Beckwith	-70	5.2
3	(512, 512, 1)	0.00	0.39	60	80	1.4	Beckwith	-70	5.2
4	(512, 512, 1)	0.00	0.41	62	80	1.4	DSHARP	-70	5.2
5	(512, 512, 1)	0.00	0.55	62	80	1.4	DSHARP	-70	5.2
6	(512, 512, 1)	0.20	0.39	60	80	1.4	Beckwith	-70	5.2
7	(256, 256, 1)	0.20	0.39	60	80	1.9	Beckwith	-70	5.2
8	(512, 512, 1)	0.20	0.41	62	80	1.4	DSHARP	-70	5.2
9	(256, 256, 1)	0.20	0.45	60	80	1.9	Beckwith	-70	5.2
10	(512, 512, 1)	0.20	0.55	62	80	1.4	DSHARP	-70	5.2
11	(512, 512, 1)	0.20	0.68	62	80	1.4	DSHARP	-70	5.2
12	(256, 256, 1)	0.25	0.03	60	80	5.1	Beckwith	-70	5.2
13	(256, 256, 1)	0.25	0.06	60	80	2.9	Beckwith	-70	5.2
14	(256, 256, 1)	0.25	0.13	60	80	2.3	Beckwith	-70	5.2
15	(256, 256, 1)	0.25	0.19	60	80	2.0	Beckwith	-70	5.2
16	(512, 512, 1)	0.25	0.20	62	80	1.4	DSHARP	-70	5.2
17	(256, 256, 1)	0.25	0.26	60	80	1.9	Beckwith	-70	5.2
18	(512, 512, 1)	0.25	0.27	62	80	1.4	DSHARP	-70	5.2
19	(256, 256, 1)	0.25	0.32	60	80	1.9	Beckwith	-70	5.2
20	(512, 512, 1)	0.25	0.39	60	80	1.4	Beckwith	-70	5.2
21	(512, 512, 1)	0.25	0.39	60	80	1.9	Beckwith	-70	5.2
22	(512, 512, 1)	0.25	0.39	60	80	1.9	DSHARP	-70	5.2
23	(512, 512, 1)	0.25	0.39	60	80	1.9	Beckwith	-70	20.0
24	(512, 512, 1)	0.25	0.39	60	80	1.9	Beckwith	-72	20.0
25	(512, 512, 1)	0.25	0.39	60	80	1.9	Beckwith	-74	20.0
26	(512, 512, 1)	0.25	0.39	60	80	0.0	Beckwith	-70	5.2
27	(512, 512, 1)	0.25	0.39	60	80	0.0	Beckwith	-70	20.0
28	(512, 512, 1)	0.25	0.41	62	80	1.4	DSHARP	-70	5.2
29	(512, 512, 1)	0.25	0.45	60	80	1.7	Beckwith	-70	5.2
30	(512, 512, 1)	0.25	0.45	60	80	1.7	Beckwith	-72	5.2
31	(512, 512, 1)	0.25	0.45	60	80	1.7	Beckwith	-75	5.2
32	(256, 256, 1)	0.25	0.45	60	80	1.9	Beckwith	-70	5.2
33	(512, 512, 1)	0.25	0.55	62	80	1.4	DSHARP	-70	5.2
34	(512, 512, 1)	0.25	0.55	62	80	0.0	DSHARP	-70	5.2
35	(512, 512, 1)	0.25	0.68	62	80	1.4	DSHARP	-70	5.2
36	(256, 256, 1)	0.30	0.06	60	80	2.9	Beckwith	-70	5.2

Table 2 continued

Table 2 (continued)

Model	Grid (r, θ, ϕ)	Flaring Index, q	M_d (M_\odot)	τ_{dust} (au)	τ_{gas} (au)	Mass Accretion Rate \dot{M} ($\times 10^{-6} M_\odot \text{ yr}^{-1}$)	Dust Opacity	Disk inclination ($^\circ$)	Stellar Luminosity (L_\odot)
37	(256, 256, 1)	0.30	0.13	60	80	2.3	Beckwith	-70	5.2
38	(256, 256, 1)	0.30	0.19	60	80	2.0	Beckwith	-70	5.2
39	(512, 512, 1)	0.30	0.20	62	80	1.4	DSHARP	-70	5.2
40	(256, 256, 1)	0.30	0.26	60	80	2.0	Beckwith	-70	5.2
41	(512, 512, 1)	0.30	0.27	62	80	1.4	DSHARP	-70	5.2
42	(512, 512, 1)	0.30	0.32	60	80	1.9	Beckwith	-68	5.2
43	(512, 512, 1)	0.30	0.32	60	80	1.9	Beckwith	-70	5.2
44	(512, 512, 1)	0.30	0.32	60	80	1.9	Beckwith	-72	5.2
45	(512, 512, 1)	0.30	0.39	60	80	1.4	Beckwith	-70	5.2
46	(512, 512, 1)	0.30	0.39	60	80	1.3	Beckwith	-70	5.2
47	(512, 512, 1)	0.30	0.39	60	80	1.2	Beckwith	-70	5.2
48	(512, 512, 1)	0.30	0.39	60	80	1.2	DSHARP	-70	5.2
49	(512, 512, 1)	0.30	0.39	60	80	0.0	Beckwith	-70	26.0
50	(512, 512, 1)	0.30	0.39	60	80	0.0	Beckwith	-70	5.2
51	(512, 512, 1)	0.30	0.39	60	80	1.5	Beckwith	-70	5.2
52	(512, 512, 1)	0.30	0.39	60	80	1.6	Beckwith	-70	5.2
53	(512, 512, 1)	0.30	0.39	60	80	1.7	Beckwith	-70	5.2
54	(512, 512, 1)	0.30	0.39	60	80	1.8	Beckwith	-70	5.2
55	(512, 512, 1)	0.30	0.39	60	80	1.7	Beckwith	-70	5.2
56	(512, 512, 1)	0.30	0.39	60	80	1.9	Beckwith	-70	5.2
57	(512, 512, 1)	0.30	0.39	60	80	1.9	DSHARP	-70	5.2
58	(512, 512, 1)	0.30	0.39	60	80	1.9	DSHARP	-72	5.2
59	(512, 512, 1)	0.30	0.39	60	80	0.0	Beckwith	-70	5.2
60	(512, 512, 1)	0.30	0.39	60	80	0.0	Beckwith	-70	52.0
61 (Fiducial)	(512, 512, 1)	0.30	0.41	62	80	1.4	DSHARP	-70	5.2
62	(512, 512, 1)	0.30	0.41	62	80	1.4	DSHARP	-72	5.2
63	(512, 512, 1)	0.30	0.41	62	80	1.4	Beckwith	-70	5.2
64	(512, 512, 1)	0.30	0.41	62	80	1.4	OH5	-70	5.2
65	(512, 512, 1)	0.30	0.41	62	80	1.4	Semenov03	-70	5.2
66	(512, 512, 1)	0.30	0.41	62	80	0.0	DSHARP	-70	5.2
67	(512, 512, 1)	0.30	0.41	62	80	0.0	DSHARP	-70	26.0
68	(512, 512, 1)	0.30	0.41	62	80	0.0	Beckwith	-70	5.2
69	(512, 512, 1)	0.30	0.41	62	80	0.0	Semenov03	-70	5.2
70	(512, 512, 1)	0.30	0.41	62	80	0.0	OH5	-70	5.2
71	(512, 512, 1)	0.30	0.45	60	80	1.9	Beckwith	-70	5.2
72	(512, 512, 1)	0.30	0.45	60	80	1.9	DSHARP	-70	5.2
73	(512, 512, 1)	0.30	0.55	62	80	1.4	DSHARP	-70	5.2
74	(512, 512, 1)	0.30	0.60	62	62	1.4	DSHARP	-70	5.2
75	(512, 512, 1)	0.30	0.60	60	60	1.4	Beckwith	-70	5.2

Table 2 continued

Table 2 (continued)

Model	Grid (r, θ, ϕ)	Flaring Index, q	M_d (M_\odot)	r_{dust} (au)	r_{gas} (au)	Mass Accretion Rate \dot{M} ($\times 10^{-6} M_\odot \text{ yr}^{-1}$)	Dust Opacity	Disk inclination ($^\circ$)	Stellar Luminosity (L_\odot)
76	(512, 512, 1)	0.30	0.60	80	80	1.4	DSHARP	-70	5.2
77	(512, 512, 1)	0.30	0.60	60	60	1.9	Beckwith	-70	5.2
78	(512, 512, 1)	0.30	0.68	62	80	1.4	DSHARP	-70	5.2
79	(512, 512, 1)	0.30	0.80	60	60	1.4	OH5	-70	5.2
80	(512, 512, 1)	0.30	0.80	60	60	1.4	Semenov03	-70	5.2
81	(256, 256, 1)	0.35	0.06	60	80	4.0	Beckwith	-70	5.2
82	(512, 512, 1)	0.35	0.27	62	80	1.4	DSHARP	-70	5.2
83	(512, 512, 1)	0.35	0.32	60	80	1.9	Beckwith	-70	5.2
84	(512, 512, 1)	0.35	0.39	60	80	1.4	Beckwith	-70	5.2
85	(512, 512, 1)	0.35	0.41	62	80	1.4	DSHARP	-70	5.2
86	(512, 512, 1)	0.35	0.55	62	80	1.4	DSHARP	-70	5.2
87	(256, 256, 1)	0.40	0.03	60	80	5.0	Beckwith	-70	5.2
88	(256, 256, 1)	0.40	0.06	60	80	2.9	Beckwith	-70	5.2
89	(256, 256, 1)	0.40	0.13	60	80	2.3	Beckwith	-70	5.2
90	(256, 256, 1)	0.40	0.19	60	80	2.1	Beckwith	-70	5.2
91	(256, 256, 1)	0.40	0.19	60	80	0.0	Beckwith	-70	5.2
92	(256, 256, 1)	0.40	0.26	60	80	2.2	Beckwith	-70	5.2
93	(512, 512, 1)	0.40	0.27	62	80	1.4	DSHARP	-70	5.2
94	(512, 512, 1)	0.40	0.41	62	80	1.4	DSHARP	-70	5.2
95	(512, 512, 1)	0.45	0.27	62	80	1.4	DSHARP	-70	5.2
96	(256, 256, 1)	0.50	0.06	60	80	3.0	Beckwith	-70	5.2
97	(256, 256, 1)	0.50	0.13	60	80	2.4	Beckwith	-70	5.2
98	(256, 256, 1)	0.50	0.19	60	80	2.0	Beckwith	-70	5.2
99	(256, 256, 1)	0.60	0.06	60	80	3.0	Beckwith	-70	5.2
100 (simobserve)	(512, 512, 1)	0.30	0.41	62	80	1.4	DSHARP	-70	5.2
101 (simobserve)	(512, 512, 1)	0.30	0.41	62	62	1.4	DSHARP	-70	5.2
102 (simobserve)	(512, 512, 1)	0.30	0.41	80	80	1.4	DSHARP	-70	5.2

Software: CASA (McMullin et al. 2007), matplotlib (Hunter 2007), RADMC-3D (Dullemond 2012), bettermoments (Teague & Foreman-Mackey 2018; Teague 2019), PVextractor (Ginsburg et al. 2016), APLpy (Ro-

bitaille & Bressert 2012; Robitaille 2019), SLAM (Aso & Sai 2023), astropy (Astropy Collaboration et al. 2022)

Facility: ALMA

REFERENCES

- Añez-López, N., Osorio, M., Busquet, G., et al. 2020, *ApJ*, 888, 41, doi: [10.3847/1538-4357/ab5dbc](https://doi.org/10.3847/1538-4357/ab5dbc)
- Alarcón, F., Casassus, S., Lyra, W., Pérez, S., & Cieza, L. 2023, *MNRAS*, doi: [10.1093/mnras/stad3734](https://doi.org/10.1093/mnras/stad3734)
- Andrews, S. M. 2020, *ARA&A*, 58, 483, doi: [10.1146/annurev-astro-031220-010302](https://doi.org/10.1146/annurev-astro-031220-010302)
- Andrews, S. M., Rosenfeld, K. A., Wilner, D. J., & Bremer, M. 2011, *ApJL*, 742, L5, doi: [10.1088/2041-8205/742/1/L5](https://doi.org/10.1088/2041-8205/742/1/L5)
- Andrews, S. M., Wilner, D. J., Hughes, A. M., et al. 2012, *ApJ*, 744, 162, doi: [10.1088/0004-637X/744/2/162](https://doi.org/10.1088/0004-637X/744/2/162)
- Andrews, S. M., Huang, J., Pérez, L. M., et al. 2018, *ApJL*, 869, L41, doi: [10.3847/2041-8213/aaf741](https://doi.org/10.3847/2041-8213/aaf741)
- Ansdell, M., Williams, J. P., Trapman, L., et al. 2018, *ApJ*, 859, 21, doi: [10.3847/1538-4357/aab890](https://doi.org/10.3847/1538-4357/aab890)
- Armitage, P. 2017, *Magnetic Fields and Self-Gravity in Early Protostellar Disks*, NASA Proposal id.17-ATP17-107
- Aso, Y., & Sai, J. 2023, *jinshisai/SLAM: First Release of SLAM, v1.0.0*, Zenodo, doi: [10.5281/zenodo.7783868](https://doi.org/10.5281/zenodo.7783868)
- Aso, Y., Ohashi, N., Saigo, K., et al. 2015, *ApJ*, 812, 27, doi: [10.1088/0004-637X/812/1/27](https://doi.org/10.1088/0004-637X/812/1/27)
- Aso, Y., Kwon, W., Ohashi, N., et al. 2023, *ApJ*, 954, 101, doi: [10.3847/1538-4357/ace624](https://doi.org/10.3847/1538-4357/ace624)
- Astropy Collaboration, Price-Whelan, A. M., Lim, P. L., et al. 2022, *ApJ*, 935, 167, doi: [10.3847/1538-4357/ac7c74](https://doi.org/10.3847/1538-4357/ac7c74)
- Baek, G., MacFarlane, B. A., Lee, J.-E., et al. 2020, *ApJ*, 895, 27, doi: [10.3847/1538-4357/ab8ad4](https://doi.org/10.3847/1538-4357/ab8ad4)
- Beckwith, S. V. W., Sargent, A. I., Chini, R. S., & Guesten, R. 1990, *AJ*, 99, 924, doi: [10.1086/115385](https://doi.org/10.1086/115385)
- Birnstiel, T., Dullemond, C. P., Zhu, Z., et al. 2018, *ApJL*, 869, L45, doi: [10.3847/2041-8213/aaf743](https://doi.org/10.3847/2041-8213/aaf743)
- Bosman, A. D., Bergin, E. A., Loomis, R. A., et al. 2021, *ApJS*, 257, 15, doi: [10.3847/1538-4365/ac1433](https://doi.org/10.3847/1538-4365/ac1433)
- Contreras Peña, C., Johnstone, D., Baek, G., et al. 2020, *MNRAS*, 495, 3614, doi: [10.1093/mnras/staa1254](https://doi.org/10.1093/mnras/staa1254)
- Crapsi, A., Caselli, P., Walmsley, C. M., et al. 2004, *A&A*, 420, 957, doi: [10.1051/0004-6361:20035915](https://doi.org/10.1051/0004-6361:20035915)
- D’Alessio, P., Cantó, J., Calvet, N., & Lizano, S. 1998, *ApJ*, 500, 411, doi: [10.1086/305702](https://doi.org/10.1086/305702)
- Draine, B. T., & Lee, H. M. 1984, *ApJ*, 285, 89, doi: [10.1086/162480](https://doi.org/10.1086/162480)
- Dullemond, C. P. 2012, *Astrophysics Source Code Library*, 1202.015. <http://adsabs.harvard.edu/abs/2012ascl.soft02015D>
- Facchini, S., van Dishoeck, E. F., Manara, C. F., et al. 2019, *A&A*, 626, L2, doi: [10.1051/0004-6361/201935496](https://doi.org/10.1051/0004-6361/201935496)
- Flores, C., Ohashi, N., Tobin, J. J., & eDisk Team. 2023, *ApJ*, in press
- Galli, P. A. B., Bouy, H., Olivares, J., et al. 2020, *A&A*, 634, A98, doi: [10.1051/0004-6361/201936708](https://doi.org/10.1051/0004-6361/201936708)
- Ginsburg, A., Robitaille, T., & Beaumont, C. 2016, *pvextractor: Position-Velocity Diagram Extractor*, *Astrophysics Source Code Library*, record ascl:1608.010. <http://ascl.net/1608.010>
- Groppi, C. E., Hunter, T. R., Blundell, R., & Sandell, G. 2007, *ApJ*, 670, 489, doi: [10.1086/521875](https://doi.org/10.1086/521875)
- Han, I., Kwon, W., Aso, Y., Bae, J., & Sheehan, P. 2023a, *ApJ*, 956, 9, doi: [10.3847/1538-4357/acf853](https://doi.org/10.3847/1538-4357/acf853)
- Han, I., Kwon, W., Aso, Y., & eDisk Team. 2023b, *ApJ*, in prep.
- Hartmann, L., Boss, A., Calvet, N., & Whitney, B. 1994, *ApJL*, 430, L49, doi: [10.1086/187435](https://doi.org/10.1086/187435)
- Hu, X., Li, Z.-Y., Zhu, Z., & Yang, C.-C. 2022, *MNRAS*, 516, 2006, doi: [10.1093/mnras/stac1799](https://doi.org/10.1093/mnras/stac1799)
- Hughes, A. M., Wilner, D. J., Qi, C., & Hogerheijde, M. R. 2008, *ApJ*, 678, 1119, doi: [10.1086/586730](https://doi.org/10.1086/586730)
- Hunter, J. D. 2007, *Computing in Science and Engineering*, 9, 90, doi: [10.1109/MCSE.2007.55](https://doi.org/10.1109/MCSE.2007.55)
- Ichikawa, T., Kido, M., Takaishi, D., et al. 2021, *ApJ*, 919, 55, doi: [10.3847/1538-4357/ac0dc3](https://doi.org/10.3847/1538-4357/ac0dc3)
- Kido, M., Takakuwa, S., Saigo, K., et al. 2023, *ApJ*, 953, 190, doi: [10.3847/1538-4357/acdd7a](https://doi.org/10.3847/1538-4357/acdd7a)
- Kwon, W., Looney, L. W., Mundy, L. G., & Welch, W. J. 2015, *ApJ*, 808, 102, doi: [10.1088/0004-637X/808/1/102](https://doi.org/10.1088/0004-637X/808/1/102)
- Lee, C.-F., Li, Z.-Y., Ho, P. T. P., et al. 2017, *Science Advances*, 3, e1602935, doi: [10.1126/sciadv.1602935](https://doi.org/10.1126/sciadv.1602935)
- Lin, Z.-Y. D., Lee, C.-F., Li, Z.-Y., Tobin, J. J., & Turner, N. J. 2021, *MNRAS*, 501, 1316, doi: [10.1093/mnras/staa3685](https://doi.org/10.1093/mnras/staa3685)
- Lin, Z.-Y. D., Li, Z.-Y., Yang, H., et al. 2020, *MNRAS*, 496, 169, doi: [10.1093/mnras/staa1499](https://doi.org/10.1093/mnras/staa1499)
- . 2022, *MNRAS*, 512, 3922, doi: [10.1093/mnras/stac753](https://doi.org/10.1093/mnras/stac753)
- . 2023a, *MNRAS*, 520, 1210, doi: [10.1093/mnras/stad173](https://doi.org/10.1093/mnras/stad173)

- Lin, Z.-Y. D., Li, Z.-Y., Tobin, J. J., et al. 2023b, *ApJ*, 951, 9, doi: [10.3847/1538-4357/acd5c9](https://doi.org/10.3847/1538-4357/acd5c9)
- Lindberg, J. E., & Jørgensen, J. K. 2012, *A&A*, 548, A24, doi: [10.1051/0004-6361/201219603](https://doi.org/10.1051/0004-6361/201219603)
- Lindberg, J. E., Jørgensen, J. K., Green, J. D., et al. 2014a, *A&A*, 565, A29, doi: [10.1051/0004-6361/201322184](https://doi.org/10.1051/0004-6361/201322184)
- Lindberg, J. E., Jørgensen, J. K., Brinch, C., et al. 2014b, *A&A*, 566, A74, doi: [10.1051/0004-6361/201322651](https://doi.org/10.1051/0004-6361/201322651)
- Liu, S.-F., Jin, S., Li, S., Isella, A., & Li, H. 2018, *ApJ*, 857, 87, doi: [10.3847/1538-4357/aab718](https://doi.org/10.3847/1538-4357/aab718)
- Mathis, J. S., Rumpl, W., & Nordsieck, K. H. 1977, *ApJ*, 217, 425, doi: [10.1086/155591](https://doi.org/10.1086/155591)
- McMullin, J. P., Waters, B., Schiebel, D., Young, W., & Golap, K. 2007, *Astronomical Data Analysis Software and Systems XVI*, 376, 127
- Mendoza, S., Cantó, J., & Raga, A. C. 2004, *RMxAA*, 40, 147. <https://arxiv.org/abs/astro-ph/0401426>
- Momose, M., Ohashi, N., Kawabe, R., Nakano, T., & Hayashi, M. 1998, *ApJ*, 504, 314, doi: [10.1086/306061](https://doi.org/10.1086/306061)
- Narayanan, S., Williams, J. P., Tobin, J. J., & eDisk Team. 2023, *ApJ*, in press
- Ohashi, N., Saigo, K., Aso, Y., et al. 2014, *ApJ*, 796, 131, doi: [10.1088/0004-637X/796/2/131](https://doi.org/10.1088/0004-637X/796/2/131)
- Ohashi, N., Tobin, J. J., Jørgensen, J. K., et al. 2023, *ApJ*, 951, 8, doi: [10.3847/1538-4357/acd384](https://doi.org/10.3847/1538-4357/acd384)
- Ossenkopf, V., & Henning, T. 1994, *A&A*, 291, 943
- Panić, O., Hogerheijde, M. R., Wilner, D., & Qi, C. 2009, *A&A*, 501, 269, doi: [10.1051/0004-6361/200911883](https://doi.org/10.1051/0004-6361/200911883)
- Peterson, D. E., Caratti o Garatti, A., Bourke, T. L., et al. 2011, *ApJS*, 194, 43, doi: [10.1088/0067-0049/194/2/43](https://doi.org/10.1088/0067-0049/194/2/43)
- Pinte, C., Dent, W. R. F., Ménard, F., et al. 2016, *ApJ*, 816, 25, doi: [10.3847/0004-637X/816/1/25](https://doi.org/10.3847/0004-637X/816/1/25)
- Pringle, J. E. 1981, *ARA&A*, 19, 137, doi: [10.1146/annurev.aa.19.090181.001033](https://doi.org/10.1146/annurev.aa.19.090181.001033)
- Robitaille, T. 2019, *APLpy v2.0: The Astronomical Plotting Library in Python*, doi: [10.5281/zenodo.2567476](https://doi.org/10.5281/zenodo.2567476)
- Robitaille, T., & Bressert, E. 2012, *APLpy: Astronomical Plotting Library in Python, Astrophysics Source Code Library*. <http://ascl.net/1208.017>
- Sai, J., Yen, H.-W., Ohashi, N., et al. 2023, *ApJ*, 954, 67, doi: [10.3847/1538-4357/ace52d](https://doi.org/10.3847/1538-4357/ace52d)
- Santamaría-Miranda, A., De Gregorio-Monsalvo, I., Plunkett, A. L., & eDisk Team. 2023, *ApJ*, in preparation
- Schöier, F. L., van der Tak, F. F. S., van Dishoeck, E. F., & Black, J. H. 2005, *A&A*, 432, 369, doi: [10.1051/0004-6361:20041729](https://doi.org/10.1051/0004-6361:20041729)
- Semenov, D., Henning, T., Helling, C., Ilgner, M., & Sedlmayr, E. 2003, *A&A*, 410, 611, doi: [10.1051/0004-6361:20031279](https://doi.org/10.1051/0004-6361:20031279)
- Sharma, R., Jørgensen, J. K., Gavino, S., et al. 2023, *ApJ*, 954, 69, doi: [10.3847/1538-4357/ace35c](https://doi.org/10.3847/1538-4357/ace35c)
- Tang, Y.-W., Dutrey, A., Koch, P. M., et al. 2023, *ApJL*, 947, L5, doi: [10.3847/2041-8213/acc45b](https://doi.org/10.3847/2041-8213/acc45b)
- Teague, R. 2019, *Research Notes of the American Astronomical Society*, 3, 74, doi: [10.3847/2515-5172/ab2125](https://doi.org/10.3847/2515-5172/ab2125)
- Teague, R., & Foreman-Mackey, D. 2018, *Research Notes of the American Astronomical Society*, 2, 173, doi: [10.3847/2515-5172/aae265](https://doi.org/10.3847/2515-5172/aae265)
- Thieme, T. J., Lai, S.-P., Ohashi, N., et al. 2023, *ApJ*, in press
- Tobin, J. J., van't Hoff, M. L. R., Leemker, M., et al. 2023, *Nature*, 615, 227, doi: [10.1038/s41586-022-05676-z](https://doi.org/10.1038/s41586-022-05676-z)
- Trapman, L., Facchini, S., Hogerheijde, M. R., van Dishoeck, E. F., & Bruderer, S. 2019, *A&A*, 629, A79, doi: [10.1051/0004-6361/201834723](https://doi.org/10.1051/0004-6361/201834723)
- Ulrich, R. K. 1976, *ApJ*, 210, 377, doi: [10.1086/154840](https://doi.org/10.1086/154840)
- van 't Hoff, M. L. R., Tobin, J. J., Trapman, L., et al. 2018, *ApJL*, 864, L23, doi: [10.3847/2041-8213/aadb8a](https://doi.org/10.3847/2041-8213/aadb8a)
- van't Hoff, M. L. R., Tobin, J. J., Li, Z.-Y., et al. 2023, *ApJ*, 951, 10, doi: [10.3847/1538-4357/accf87](https://doi.org/10.3847/1538-4357/accf87)
- Villenave, M., Ménard, F., Dent, W. R. F., et al. 2020, *A&A*, 642, A164, doi: [10.1051/0004-6361/202038087](https://doi.org/10.1051/0004-6361/202038087)
- Villenave, M., Stapelfeldt, K. R., Duchêne, G., et al. 2022, *ApJ*, 930, 11, doi: [10.3847/1538-4357/ac5fae](https://doi.org/10.3847/1538-4357/ac5fae)
- Yamato, Y., Aikawa, Y., Ohashi, N., et al. 2023, *ApJ*, 951, 11, doi: [10.3847/1538-4357/accd71](https://doi.org/10.3847/1538-4357/accd71)
- Yang, H., & Li, Z.-Y. 2020, *ApJ*, 889, 15, doi: [10.3847/1538-4357/ab5f08](https://doi.org/10.3847/1538-4357/ab5f08)
- Yang, H., Li, Z.-Y., Looney, L., & Stephens, I. 2016, *MNRAS*, 456, 2794, doi: [10.1093/mnras/stv2633](https://doi.org/10.1093/mnras/stv2633)
- Yang, H., Li, Z.-Y., Looney, L. W., Girart, J. M., & Stephens, I. W. 2017, *MNRAS*, 472, 373, doi: [10.1093/mnras/stx1951](https://doi.org/10.1093/mnras/stx1951)
- Yen, H.-W., Takakuwa, S., Ohashi, N., et al. 2014, *ApJ*, 793, 1, doi: [10.1088/0004-637X/793/1/1](https://doi.org/10.1088/0004-637X/793/1/1)
- Yoon, S.-Y., Lee, J.-E., Lee, S., et al. 2021, *ApJ*, 919, 116, doi: [10.3847/1538-4357/ac1358](https://doi.org/10.3847/1538-4357/ac1358)